



HAL
open science

Mixing of non-Newtonian inelastic fluid in a turbulent patch of T-junction

Haining Luo, Alexandre Delache, Serge Simoëns

► **To cite this version:**

Haining Luo, Alexandre Delache, Serge Simoëns. Mixing of non-Newtonian inelastic fluid in a turbulent patch of T-junction. *Journal of Non-Newtonian Fluid Mechanics*, 2020, 10.1016/j.jnnfm.2020.104307 . hal-02890080

HAL Id: hal-02890080

<https://hal.science/hal-02890080>

Submitted on 6 Jul 2020

HAL is a multi-disciplinary open access archive for the deposit and dissemination of scientific research documents, whether they are published or not. The documents may come from teaching and research institutions in France or abroad, or from public or private research centers.

L'archive ouverte pluridisciplinaire **HAL**, est destinée au dépôt et à la diffusion de documents scientifiques de niveau recherche, publiés ou non, émanant des établissements d'enseignement et de recherche français ou étrangers, des laboratoires publics ou privés.

Mixing of non-Newtonian inelastic fluid in a turbulent patch of T-junction

Haining Luo^{a,*}, Alexandre Delache^b, Serge Simoëns^a

^a *LMFA - Université de Lyon, UMR CNRS 5509, Ecole Centrale de Lyon, INSA Lyon, UCB Lyon I, 69130, Ecully, France*

^b *LMFA - site de Saint-Etienne, Université de Lyon, Université Jean Monnet de Saint-Etienne, 42023 Saint-Etienne - France*

In this paper, we present result from a direct numerical simulation (DNS) of turbulent flow in a converging T-junction for both Newtonian (water) and non-Newtonian inelastic fluid (dilute Xanthan Gum solution). Based on experimental data, the Bird-Carreau law is used to capture the inelastic shear thinning property of the solution. For the Xanthan solution, the viscosity at rest is about 100 times greater than the viscosity at high shear-rate. A passive scalar is introduced in the transverse branch to investigate the mixing in such configuration. The nominal Reynolds number at the exit varies from 4800 to 8000 for the Newtonian cases and for the same inflow rates, the non-Newtonian flow will be necessarily at lower nominal Reynolds number. Two regimes are explored as a function of the inlet velocity ratio $r = U_b/U_m$: the "deflecting" regime noted DR ($r = 1$) and the "impinging" regime noted IR ($r = 4$). For the non-Newtonian cases, two viscous cores are observed before the junction. After the junction a laminar state is obtained for the lower flow rate conditions. Surprisingly, in spite of a large viscosity at rest, a self-sustained non-Newtonian turbulence is achieved except for one case. We describe existing vortex mechanisms which pilot the scalar mixing. In addition, we show that in the non-Newtonian cases, the existing peak of turbulence is only shifted in the DR case. The shift is probably due to the nature of the fluid and not to the dynamical regime. After an intense turbulent zone, we show that a re-laminarization zone appears in the non-Newtonian case which reduces the fluctuation as well as mixing. As a result, IR has a better mixing quality than DR.

1. Introduction

Flows in T-junction configurations are encountered in various industrial applications and physiological situations such as piping systems in nuclear power plants [1, 2], automobile air-conditioning system [3], chemical reactors [4, 5], combustion chambers [6] and hemodynamic studies [7–9] among others.

*Corresponding author

Email address: haining_luo@hotmail.com (Haining Luo)

For T-junction configurations, there are two main flow cases depending on the number of inlet: diverging and converging flow configurations. A diverging flow has one inlet and two outlets [10–16] whereas a converging flow has two inlets and one outlet in order to mix the two inlet flows (see Figure 2). Other variations can also be accounted : due to different angles between inlet and outlet pipe axis; changing cross section shape (circular, rectangular for example); leaving the junction either sharp or with chamfer, etc. In the current work, we consider only the T-shape junction i.e with an angle of 90 degrees in converging flow configurations.

Main part of the litterature concerning non Newtonian effects studies inside T-junction flows are focused on diverging flow configurations. Most of these studies consider hemodynamics or micro-channel mixing with non-Newtonian fluid flows and low Reynolds number situations. They account for shear-thinning, viscoelasticity [8, 9, 12, 15, 17] and/or pulsating inlet condition effects [7].

Studies focusing on the converging configurations are mainly interested in macro-scale [1–3, 18–21] as the ones dedicated to nuclear power plant applications for which characteristic duct diameter is of order $100mm$. Another application concerns with milli-channels as micro-technology reactors for multiphase reactions. For example, the work by Tourvieille et al. [22] studies the gas-liquid mixing in a T-junction with a square cross-section of $2mm$ wide, filled with metal foams as catalysis material and for relatively small Reynolds numbers (the Reynolds number for the liquid phase is around 80). Few 3D Direct Numerical Simulations (DNS) are carried out for relatively high Reynolds number [18, 20, 21]. Among these studies, the nominal Reynolds numbers (based on zero shear viscosity) at the inlets range from 243 to 4485 and from 4376 to 8970 at exits which covers both laminar and turbulent regimes. Moreover, Georgiou and Papalexandris [21] take into account the variation of viscosity with temperature. Sharing the same converging flow configuration, variations on geometry are still present between litterature cases, which makes comparisons difficult : Haren [20] used circular pipes with chamfer and fillet at the junction; Both Georgiou and Papalexandris [21] and Fukushima et al. [18] used rectangular ducts without any chamfer or fillet whereas the relative inlet size ratio and the ways by which the transversal branch attaches to the main duct are different. In a T-junction configuration, concerning scalar mixing quality, three different flow regimes are proposed and found experimentally by Sroka [23] and Kamide [24]. They are distinguished via one criteria, the velocity ratio $r = U_b/U_m$ between the main longitudinal pipe velocities U_m and the transverse branch pipe U_b . In the case for which the diameter of the main pipe equals to that of the transverse branch pipe, the three different flow regimes are the "wall-jet" regime for $r < 0.07$, the "deflecting" regime (noted DR) for $0.07 < r < 1$ and the "impinging" regime (noted IR) for $r > 1$. Two fundamental flow phenomenom interests of T-junctions are the generations of a mixing layer and of a re-circulation zone inducing different flow mixing characteristics. Flows in a T-junction geometry could be considered as confined versions of the "Jet In Cross Flow" (JICF) which is the subject of extensive studies [25, 26] and for which the ratio r is $r > 1$ for most part of the studied cases. These two types of flows are demonstrated to share similar coherent structures as was shown in the work of Brucker [27] for a circular T-junction flow and in the works of Fric [28] and Haven [29] for JICF. In JICF, flow pulsations is applied to control the

penetration of the jet [30]. For such case, an optimal stroke ratio is discussed to maximize a scalar mixing. In a T-junction, flow pulsations, imposed on the two compressible gaz inlets, do not necessarily improve mixing [6].

To our knowledge, only few publications studies focus on non-Newtonian effects in the converging T-junction configuration. Nguyen's experiments [31] focused on the "deflecting" regime $r = 1$ for both Xanthan Gum (XG) and Polyacrylamid (PAA) (both non-Newtonian) solutions in a converging T-junction with circular pipes of $D = 8mm$ diameter. While the two initial converging currents remain highly viscous and laminar before the junction, in a non-obvious way, the flow becomes turbulent after the junction. This turbulence is obtained at relatively low Reynolds numbers from ~ 10 to 50 (based on the pipe diameter, the inlet velocity (for three cases) and the zero shear viscosity (at rest)). The fact that XG has a negligible elasticity, in contrast to PAA [32] suggests that the turbulent regime is due to shear thinning effects, dominant for an XG solution. Moreover by comparing the flow with the XG solution to the one with a Newtonian fluid (water) flow, Nguyen observed a downstream-wise shifting of the turbulence peak. The present investigation aims to confirm these preliminary observations. In addition to the "deflecting" regime ($r = 1$), we have investigated the "impinging" regime ($r = 4$) which is not present in his experimental study.

Nevertheless our main objectives are to describe the non-Newtonian mechanisms that allow a scalar to mix in such converging geometry and to quantify this mixing [23] as a function of the different dynamic regimes. The mixing quality is directly related to the presence of turbulence developing from the viscous core located at the junction. Compared to the Newtonian flow, in the non-Newtonian case the junction zone has an additional specificity. Indeed, from the junction, near the recirculation zone, the shear considerably reduces the viscosity to values close to the Newtonian viscosity. This causes a strong turbulent puff which improves the mixing of the scalar. At the opposite, beyond the junction, the shear decreases, resulting in a significant increase of viscosity, which can lead to a zone of relaminarization that prevents mixing.

It is thus not obvious to predict how the mixing will behave both for the non-Newtonian and for the Newtonian fluid cases as a function of the different regimes (IR and DR). To clarify this, we have performed Direct Numerical Simulations for low and moderate Reynolds numbers for XG water solution and Newtonian fluid (water) corresponding to fluid cases used in Nguyen's experiments. With the present DNS we have access to the tridimensional organization of the flows and the associated turbulent phenomena that enhance the scalar mixing. To avoid numerical problems associated with meshing at junction, particularly for the non-Newtonian fluid flow cases, we consider a square cross section. We do think that the phenomena observed in the experiments, where the cross-section is circular, are significant enough to be predominant considering mixing for the present square geometry.

In section 2, we describe the rheological model including the governing equations. We provide also mesh analysis and simulation parameters. In section 3, we describe the non-Newtonian organization of the flow, focusing on the behavior differences between deflecting and impinging regimes. Section 4 describes the development of the non-Newtonian turbulence production from the two viscous cores, the possible re-laminarizations as well as the turbulence peak shifting for the deflecting regime. Passive scalar mixing influenced by

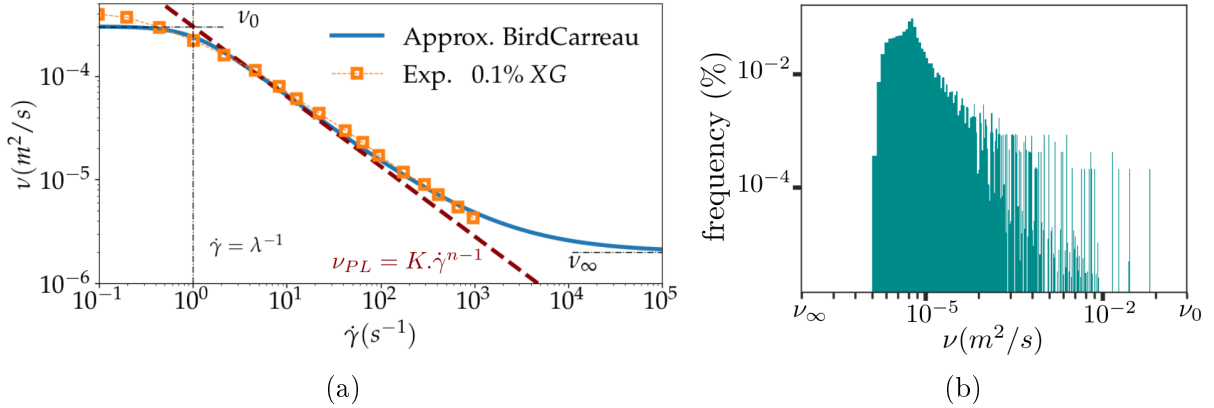


Figure 1: (a) best fitting Bird-Carreau (BC) Law (equation 1c) from the Nguyen’s experimental work [31], used for the present DNS. It shows the transition from ν_0 to ν_∞ as a function of shear. Law parameters are $n = 0.326$, $\lambda = 1s$ and $\alpha = 2$. (b) Example of an histogram of the viscosity, here obtained from all the values on a transversal planar DNS cut in the main pipe just before the junction for the case NN_d^2 (see Table 2). Viscosity range, from ν_∞ to ν_0 , is shown on the x axis. Frequency (percentage of all values on an interval comparing to all used values) is on the y axis.

turbulence and its evolution along the main flow direction is finally analyzed.

2. Rheological model

2.1. Governing Equation

For DNS non Newtonian fluid viscosity, we take the one of the XG shear thinning solution used in Nguyen’s work [31] for studying the converging T junction configuration (figure 1a). XG has a very effective thickening nature which increases the initial viscosity of the carrier fluid and is often used as a stabilizer. Adding XG to water will make the solution very viscous as a function of its concentration. In our case, the viscosity of the XG solution at rest ν_0 is 100 times more viscous than pure water. When shear is applied to an XG solution, its viscosity will decrease (shear thinning effect) as a function of increasing shear until reaching its lower viscosity limit ν_∞ close to the viscosity of the carrier fluid. Here we have $\nu_0 = 3 \times 10^{-4}m^2/s$ and $\nu_\infty = 2 \times 10^{-6}m^2/s$ (figure 1a and 1b). To describe flows with such solutions, we use for numerical simulation, the Navier-Stokes equations (without gravity effect) (equations 1a and 1b) combined with the Bird-Carreau (BC) Law (equation 1c). We further implement the mass transport equation (equation 1d) for a passive scalar c transported by the flow from one inlet (transverse branch) :

$$\frac{\partial \mathbf{u}}{\partial t} + \mathbf{u} \cdot \nabla \mathbf{u} = -\nabla p^* + \nabla \cdot \nu_s \nabla \mathbf{u} \quad (1a)$$

$$\nabla \cdot \mathbf{u} = 0 \quad (1b)$$

$$\nu_s(\dot{\gamma}) = \nu_\infty + (\nu_0 - \nu_\infty)[1 + (\lambda\dot{\gamma})^\alpha]^{-\frac{n-1}{\alpha}} \quad (1c)$$

$$\frac{\partial c}{\partial t} + \mathbf{u} \cdot \nabla c = D_c \Delta c \quad (1d)$$

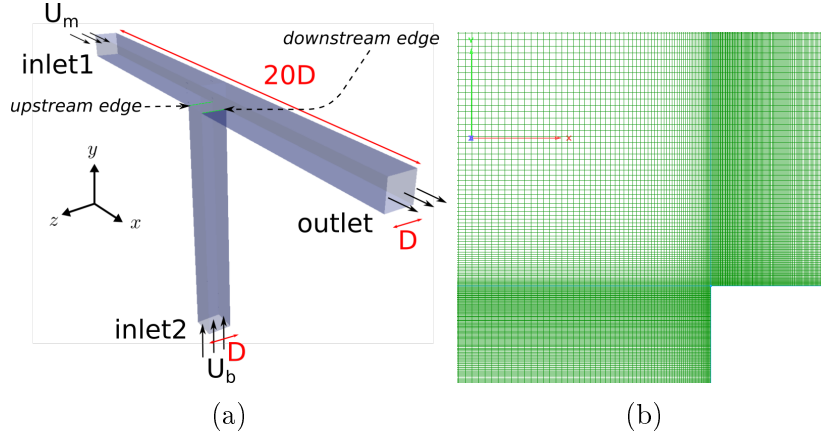


Figure 2: (a) Computational domain for the T-junction mixing with two inlets and one outlet. The square-shaped cross section has a side width D equal to $8mm$. (b) Mesh details at a cut over plane (x, y) at $z = 0$ (pipe center) on the downstream edge.

where p^* is the kinematic pressure and ν_s is the kinematic viscosity depending on the local shear rate $\dot{\gamma} = (2\mathbf{s} : \mathbf{s})^{1/2}$ with the strain rate tensor \mathbf{s} defined by $\mathbf{s}_{ij} = (\partial_j \mathbf{u}_i + \partial_i \mathbf{u}_j)/2$ for which $i, j = x, y$ or z .

Concerning the BC law, the power index n reveals its power-law nature for intermediate values of the shear rate, and λ^{-1} represents a start-up threshold of strain rate for which shear thinning effects begin to take place. The fitting from the experimental curve points could not be exact. A small difference could be pointed out (figure 1a for high shear values). The experimental points didn't furnish the ν_∞ plateau due to limitation of the used rheometer to relatively low shears (under $10^3 s^{-1}$). The arbitrary fixed ν_∞ , chosen here, could not lead to noticeable numerical result changes, inducing to change our conclusions in any part of the present work. From this Bird-Carreau law, we can extract by fitting with a power law for intermediate shear rate $\nu_{PL} = K \cdot \dot{\gamma}^{n-1}$. For example, on Figure 1b, we plot the histogram of the viscosities obtained from all values on a transversal plane cut in the main pipe just before the junction, for the laminar regime computed here with DNS. As we can observe, a large range of viscosity values are far from ν_∞ .

In the case of the Newtonian fluid, water's kinematic viscosity is used in Eq. (1a) inside the term $\nabla \cdot \nu_s \nabla \mathbf{u}$. This term can then be simplified as $\nu_{water} \nabla^2 \mathbf{u}$ with $\nu_{water} = 10^{-6} m^2/s = \nu_\infty/2$. For the passive scalar, we fix its diffusivity D_c to be uniform and $D_c = \nu_{water}$ for all simulations. The complete set of parameters is presented in section 2.3.

2.2. Numerical Method

The governing equations Eq. (1a,1b) and the constitutive law Eq. (1c) are implemented in the Finite Volume based opensource code OpenFOAM which handles flows in complex geometries and different rheological models. A transient solver is applied to perform fully resolved Newtonian and non-Newtonian turbulence simulations of the start-up phases and their steady state in a fixed T-junction configuration. Inside this solver, a pressure based semi-implicit algorithm PISO is applied where the decoupling of pressure and velocity is

	U	p	c
<i>inlet1</i>	$\mathbf{u} = \mathbf{u}_x(y, z) \cdot \mathbf{n}$	$\nabla p \cdot \mathbf{n} = 0$	$c = 0$
<i>inlet2</i>	$\mathbf{u} = \mathbf{u}_y(x, z) \cdot \mathbf{n}$	$\nabla p \cdot \mathbf{n} = 0$	$c = 1$
<i>outlet</i>	$\nabla \mathbf{u} \cdot \mathbf{n} = 0$	$\nabla p = const.$	$\nabla c \cdot \mathbf{n} = 0$
<i>wall</i>	$\mathbf{u} = 0$	$\nabla p \cdot \mathbf{n} = 0$	$\nabla c \cdot \mathbf{n} = 0$

Table 1: Boundary conditions for DNS. \mathbf{n} is the normal vector at respective boundaries.

achieved by a velocity-predictor and pressure corrector. In those simulations, the main effort of the PISO-algorithm resides on solving the Poisson equation especially during the start-up stage. We apply a fixed time step Δt that is set to be 5 or 10 times smaller in start-up phases than what we use once the solutions converge. The maximum CFL number of all computations is held below 0.35 for all simulations, which leads to a Δt of $10^{-6}s$. In our simulations, the total cell number is around 25 million and parallel simulations are carried out on 480 cores. The decomposition algorithm "scotch" is used and we have 50000 cells per core which is twice the prescribed optimal number given in the notes by Axtmann et al. [33] and Guerrero [34].

Our computational domain for the T-junction configuration with two inlets and one outlet is shown on Figure 2 a). On this figure, we distinguish the upstream and downstream edges. The main longitudinal pipe has a length of $20D$ with D the width of the square section. The transverse branch pipe has a length of $10D$ with the same width. At $t = 0$ fluid is set to be at complete rest ($\mathbf{u} = 0$). Only *inlet1* and *inlet2* (see Figure (2a)) are forced with the laminar profile of a flow in a square duct as boundary condition to initialize the start-up. On walls the no-slip condition is applied. A fixed-value boundary condition is applied for pressure at *outlet*. We introduce a non-null passive scalar c only at *inlet2* at each time step. The imposed inlet velocity profile corresponds to a Newtonian Hagen-Poiseuille flow in a square duct [35]. For *inlet1*, we impose in the plane (y, z) :

$$\mathbf{u}_x(y, z) = \frac{\Delta p^*}{\nu L} \frac{4h^2}{\pi^3} \sum_{n=1,3,5\dots}^{\infty} \frac{1}{n^3} \left[1 - \frac{\cosh(n\pi z/D)}{\cosh(n\pi w/2D)} \right] \sin(n\pi y/D), \quad (2)$$

where $h = w = D/2$ and the first 20 terms of the series are taken into consideration to obtain a converged sum. Note that in the experimental set [31], due to the homogenization boxes at entrance of the 2 inlets, a non turbulent condition is found at $8D$ from both entrance. For each case, we adjust the coefficient $\frac{\Delta p^*}{\nu L}$ to obtain the specific bulk velocity U_{bulk} given in Table 2 ($U_{bulk} = U_m$ for *inlet1* and $U_{bulk} = U_b$ for *inlet2*). By symmetry we apply the similar inlet condition at *inlet2* (the branch inlet) named $u_y(x, z)$. For the passive scalar, we impose two symbolic values at the entrance : $c = 0$ at *inlet1* and $c = 1$ at *inlet2*. Zero gradient condition is imposed at outlet for concentration and velocity i.e $\nabla c \cdot \mathbf{n} = 0$, $\nabla \mathbf{u} \cdot \mathbf{n} = 0$ where \mathbf{n} is the normal vector at outlet. All boundary conditions are specified in Table 1 for \mathbf{u} , c and p .

Runs	$U_{bulk}(m/s)$	Fluid	r	Re_{PL}^{gen}	$\langle Re \rangle_{inlet}$	$\langle Re \rangle_{exit}$	t^*	
NN_d^1	0.3	NN	1	329	203	484	5.25	L
N_d^1	0.3	N	1	4800	2400	4800	11.25	T
NN_d^2	0.5	NN	1	773	449	1230	17.5	T
N_d^2	0.5	N	1	8000	4000	8000	18.75	T
NN_i^2	(0.2, 0.8)	NN	4	(167, 1697)	(107, 910)	1194	12.5	T
N_i^2	(0.2, 0.8)	N	4	(3200, 12800)	(1600, 6400)	8000	12.5	T

Table 2: DNS parameters where N and NN represent the Newtonian and non-Newtonian fluids, lower index d, i are the abbreviation for "deflecting" regime and "impinging" regime. $r = U_b/U_m$ denotes the velocity ratio ($inlet1$ velocity to $inlet2$ velocity). The time $t^* = \frac{t}{10D/\langle U \rangle_{exit}}$ is the real time divided by time of flow from junction to the outlet. When necessary two numbers are indicated in parenthesis for a given quantity. $U_{bulk} = U_m$ for $inlet1$ and $U_{bulk} = U_b$ for $inlet2$. This corresponds for the first one to value characteristic of the cross flow ($inlet1$) and for the second one to a value characteristic of the transversal jet ($inlet2$). There is only one value when quantities are equals for both inlets. T and L indicate the turbulent state and the laminar state, respectively. More comments are added on significance of the $\langle Re \rangle_{exit}$ in section 2.3.

2.3. Simulation Parameters

We have performed 6 simulations as listed in Table 2 where the last two are aimed to investigate the IR regime and the first four simulations are aimed to reproduce the same DR regime as in Nguyen's work [31] but using a square shaped cross section. Simulations' naming are composed with N or NN representing respectively a simulation with a Newtonian fluid (water) and with a non-Newtonian fluid (XG). At these N or NN is added an upper index with the values 1 or 2 corresponding respectively to the 2 bulk velocities $U_{bulk} = 0.3m/s$ and $0.5m/s$ treated here (as in Nguyen [31]) (remind that $U_{bulk} = U_m$ for $inlet1$ and $U_{bulk} = U_b$ for $inlet2$). Additionally are added the lower indices d or i as abbreviations for the flow regimes, respectively, "deflecting" and "impinging". As shown on figure (2), U_b denotes the velocity at entrance of the vertical branch, $inlet2$, and U_m is the velocity at the entrance of the main duct, $inlet1$. As the square-shaped cross-section is constant all along the pipes for the whole geometry, the velocity ratio defined by $r = U_b/U_m$ characterizes the flow regime as stated in the introduction : when $r = 4$, previous studies with Newtonian fluids [23, 24] confirm the IR regime; when this ratio is equal to 1, it corresponds to the DR regime.

The nominal Reynolds number at the exit (inlet) for water is defined by $\langle Re \rangle_{exit} = \langle U \rangle_{exit} D / \nu_{water}$ where the width of the square duct is $D = 8mm$ as in Nguyen's work [31] and $\langle * \rangle_{exit}$ ($\langle * \rangle_{inlet}$) denotes the spatial average value on the exit (inlet) slice at plane (y, z) for any quantity $*$. For the shear thinning XG solution, the viscosity varies in space and time along the flow. We define the spatial averaged Reynolds numbers at the inlet $\langle Re \rangle_{inlet} = \langle U \rangle_{inlet} D / \langle \nu \rangle_{inlet}$ and at the outlet $\langle Re \rangle_{exit} = \langle U \rangle_{exit} D / \langle \nu \rangle_{exit}$. At the inlet, this is computed a priori as the inlet velocity is imposed by an Hagen-Poiseuille flow with its associated shear rate and the induced viscosity. By this way we account for the variability of ν at the inlet and the at the exit (at $x/D = 9.5$). Note that the Reynolds number $\langle Re \rangle_{inlet}$ remains almost unchanged along the branches of the pipes from inlets

to the crossing zone at the junction. We can roughly say that, regarding both Newtonian and non-Newtonian cases, the average Reynolds numbers at *outlet* for all our simulations ranges from $\langle Re \rangle_{outlet} = 500$ to $\langle Re \rangle_{outlet} = 8000$. It would be not surprising for these flows to fall in the transition range between laminar and turbulent regimes. It is not easy to characterise a potential turbulent behavior of non-Newtonian fluid flows with the common form of the Reynolds number. For the non-Newtonian cases, $Re_\infty = U_{exit}D/\nu_\infty$ is the largest as possible defined Reynolds number but is not characteristic of all the flow behavior at the outlet. However, efforts have been made to improve such characterisation by introducing the generalized Reynolds number, taking a power law viscosity $\nu_{PL} = K \cdot \dot{\gamma}^n$ fitting the viscosity curve (see figure(1a)). This generalized Reynolds number is defined in the work of Madlener et al. [36] and we apply this definition to characterise the flow cases at their inlet :

$$Re_{PL}^{gen} = \frac{D^n U_{bulk}^{2-n}}{K ((3n+1)/4n)^n 8^{n-1}}$$

Values of the calculated Re_{PL}^{gen} are shown on the Table 2. Note that Re_{PL}^{gen} could be computed a priori. In the case of Newtonian fluid, we have $n = 1$ and $K = \nu_{water}$ so that the generalized Reynolds number reduces to the nominal classic Reynolds number. As we observe in Table 2, the values of Re_{PL}^{gen} are systematically bigger than those of $\langle Re \rangle_{inlet}$ but of the same order.

For the Newtonian cases, the value of the molecular diffusivity D_c of the scalar c into water, is fixed in order to have a Schmidt number : $Sc_N = \nu_{water}/D_c = 1$. Under turbulent regime hypothesis, the smallest scale for velocity is the Kolmogorov's scale η_K^N defined by $\eta_K^N = \nu_{water}^{3/4} \varepsilon_N^{-1/4}$ where ε_N is the kinetic energy dissipation rate. In such case, the smallest scalar scale ([?],[37]) is the Batchelor's scale λ_B^N defined by $\lambda_B^N = \eta_K^N / Sc_N^{1/2}$. This means, for $Sc_N = 1$, (that when the Kolmogorov's scale is fully resolved, so does the Batchelor's scale.

For non-Newtonian fluid flow, since the viscosity ν_{NN} varies according to our Bird-Carreau law (1c) then the associated Non-Newtonian Schmidt number $Sc_{NN} = \nu_{NN}/D_c$ covers a large range from 2 to 300 as $Sc_{NN} = Sc_N \frac{\nu_{NN}}{\nu_{water}}$ and $\nu_{NN} \in [2\nu_{water}, 300\nu_{water}]$. Here the molecular scalar diffusion is hypothetised the same for Newtonian and non Newtonian cases as the non Newtonian solvent is water and XG concentration is low.

If we note ε_{NN} the kinetic energy dissipation rate for non Newtonian fluid flow cases, the associated Kolmogorov's scale is related to the Newtonian one by : $\eta_K^{NN} = \eta_K^N \left(\frac{\nu_{NN}}{\nu_{water}} \right)^{3/4} \left(\frac{\varepsilon_{NN}}{\varepsilon_N} \right)^{-1/4}$, following their respective definition. Thus η_K^{NN} ($= \eta_K^N \left(\frac{\nu_{NN}}{\nu_{water}} \right)^{3/4}$) is always greater than the kolmogorov's scale of the corresponding Newtonian case and so if resolution is sufficient for Newtonian case, it is for the non Newtonian cases.

If we assume that the kinetic energy dissipation rate for non-Newtonian fluid flow case, ε_{NN} , is of the same order than the one in Newtonian fluid flow cases, i.e $\varepsilon_{NN} \simeq \varepsilon_N$ (in our case of dilute regime (low Deborah number) and negligible elastic contribution, the DNS results by De Angelis et al. ([?]) help to sustained such hypothesis), then we can conclude that we have always $\eta_K^{NN} > \eta_K^N$.

In the same way, due to their definitions, the non-Newtonian Batchelor's scale is linked to the Newtonian one by : $\lambda_B^{NN} \simeq \lambda_B^N \left(\frac{\nu_{NN}}{\nu_{water}} \right)^{3/4} > \lambda_B^N$. If the Kolmogorov's scale η_K^N is fully

resolved for a Newtonian fluid case, then the Kolmogorov's scale η_K^{NN} and the Batchelor's scale λ_B^{NN} are fully resolved for the non-Newtonian associated case. In conclusion, we shall be able to fully resolve both velocity and passive scalar field of non Newtonian cases if we do for the associated Newtonian cases.

2.4. Mesh

We manage to get a comparable meshing as for the work of Georgiou and Papalexandris [21]. As for their T-junction which is submitted to slight variations of viscosity due to temperature, we apply a refinement in the junction zone in the x and y directions. Additionally, we apply a refinement in the z direction. Every rectangular cross-section is thus discretized with 130×130 cells with refinement to walls.

The cell-spacing constraint to the wall satisfies the criteria $x^+ \approx 0.5$ (as for y^+ and z^+) in wall unit for Newtonian case (N_d^2 .) A detail of meshing is shown on Figure 2 b). The Newtonian cases are then considered fully resolved as the criteria for x^+ (and other direction) is satisfied at the wall. Given the fact that we have $\nu_\infty = 2\nu_{water}$, all non Newtonian cases are also over-resolved. The stretching ratio for the neighboring cells is kept to be constant : 1.05 in the cross-section and 1.01 streamwise. The mesh is strictly orthogonal and skew-free. The geometry is chosen to have two rather long inlet pipes and an equal length outlet pipe ($\approx 10D$) so that we can isolate possible effects between the junction and inlet/outlet boundary conditions.

3. Production of turbulent state

3.1. From laminar to turbulent state

For all simulations, $\mathbf{u}, c, \nu, \boldsymbol{\omega}$ denote respectively instantaneous velocity, concentration, kinematic viscosity and vorticity field where $\boldsymbol{\omega} = \nabla \times \mathbf{u}$. The IR and DR regimes are illustrated in Figure 3 for non-Newtonian cases NN_d^2 and NN_i^2 , where we show contour plots on plane $z = 0$ for $|\boldsymbol{\omega}|$, c and ν . By plotting the vorticity magnitude $|\boldsymbol{\omega}|$ on figures 3(a) and (b), we see different vortex scales in both cases: large-scale structures break into small ones downstream.

On figures 3(c) and (d), the concentration field is colored from red ($c = 1$ at *inlet2*) to blue ($c = 0$ at *inlet1*). We can then distinguish the DR regime (NN_d^2) from the IR regime (NN_i^2) by the color-coding of c : in the DR case (NN_d^2), the jet is only deflected and bent slowly to flow in the main longitudinal direction whereas in the IR case (NN_i^2) the jet penetrates the cross-flow resulting in a reflection at the upper wall. We observe that the separation takes place at 2 locations : one happens inside branch *inlet2* before the upstream edge due to a blocking effect from the cross-flow; another separation happens from the downstream edge forming a re-circulation bubble. At the downstream edge, the separation angle is significantly steep for the IR (NN_i^2) case which implies that the re-circulation bubble occupies more space in the transverse direction than for the DR (NN_d^2) case. As for mixing, at the junction, we see sharp boundaries between $c \approx 1$ zones and $c \approx 0$ zones. Near the outlet we observe a much more uniform distribution of c .

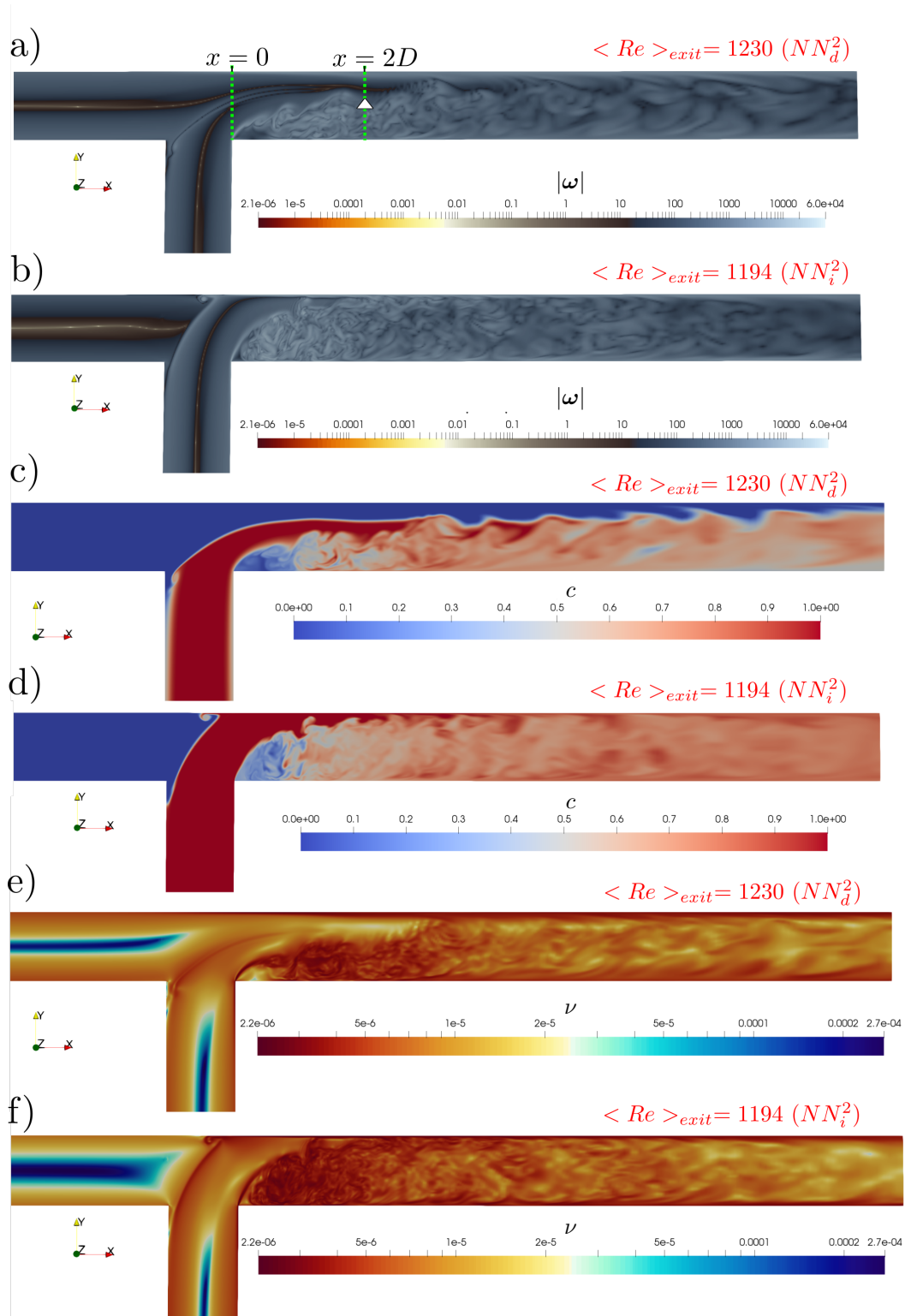


Figure 3: Contour of instantaneous quantity fields on the longitudinal plane $z = 0$ for respectively vorticity magnitude $|\omega|$, passive scalar c and viscosity ν for : deflecting case NN_d^2 a) c) e) and impinging case NN_i^2 b) d) f). The symbol \triangle represents the location of the probe corresponding to plots in figure 4.

July 1, 2020

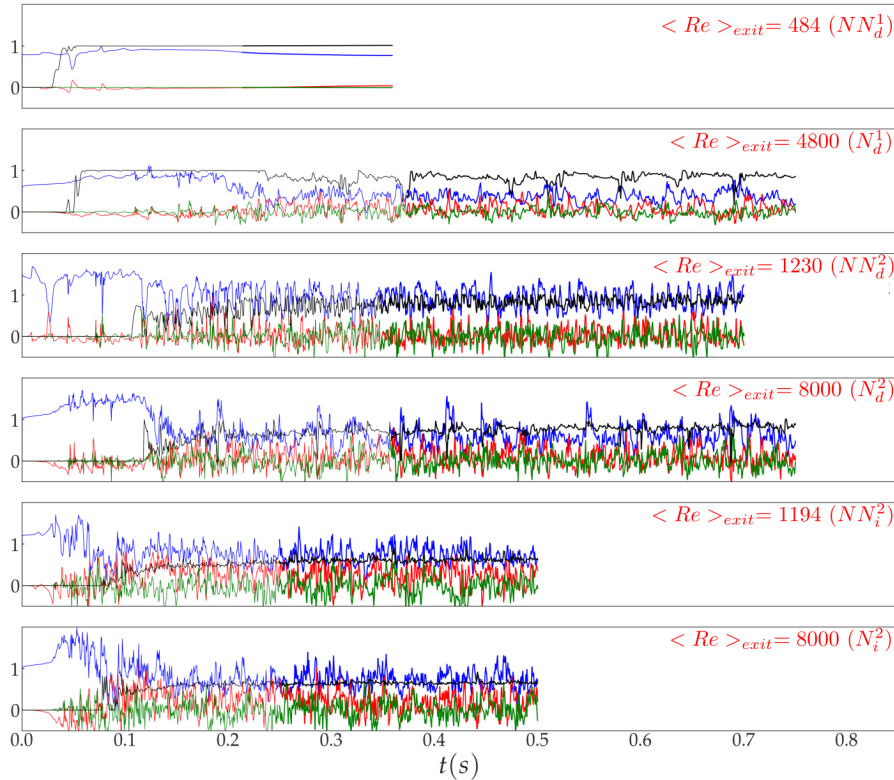


Figure 4: For 6 cases, the time history (in second) of \mathbf{u}_x , \mathbf{u}_y , \mathbf{u}_z and c at the center of slice $x/D = 2$ (corresponding to the probe indicated by \triangle in figure 3 a)) is presented. u_x , u_y , u_z and c are respectively coded by blue, red, green and black lines. Each lines have a transitional part and a statistically stationary part. The latter part is made thicker to distinguish from the former one. The horizontal axis represents the time in s and the vertical axis represents either the velocity in m/s or the concentration $0 \leq c \leq 1$ (arbitrary unit).

We observe on figures 3 e) and f) the viscosity fields ν for the IR and DR cases : two laminar flows converge at the junction, each carrying a very viscous core. The two flows meet at the junction, from both the upstream and the downstream edges, two strong shear layers are developed. As a result, in these two layers, XG solution exhibits a lower viscosity due to shear thinning. Additionally, when approaching the outlet the non-Newtonian fluid flow seems to increase its viscosity from $x/D = 2$.

Consider that, for all our 6 simulations, the Reynolds number $\langle Re \rangle_{exit}$ ranges from small to relatively large values. We have fixed a probe at $x/D = 2$ at the duct center to record mono-dimensional signals of each of our multiple variables. The figure 4 shows the time history of the three components of velocity $\mathbf{u} = (\mathbf{u}_x, \mathbf{u}_y, \mathbf{u}_z)$ and of the concentration c at the probe location.

In each of our 6 simulations, the signals of \mathbf{u}_x , \mathbf{u}_y , \mathbf{u}_z , and c begin by a value of 0 (\mathbf{u}_x , due to the imposed pressure gradient and velocity profile, has a very rapid increase) at the probe location and within a certain amount of delay, fluctuations are detected. For concentration it needs a minimum of the convection's time for the fluctuations to be detected as there is

no scalar at the probe location at $t = 0$.

For each case, each lines have a transition part (thin line) and a statistically stationary part (bold line) beginning at the given time and from which we made our statistical analysis (see after). Note that cases have non equal time of computation involving results till different times (for example the two last stop at $t = 0.5$ s.)

Quite noticeably, for the non-Newtonian the lowest flow rate, at regime DR (NN_d^1) with $\langle Re \rangle_{inlet} = 203$ ($\langle Re \rangle_{exit} = 484$), both velocity and concentration returns to a steady constant value after the initial fluctuations (see Figure 4 case NN_d^1). This means that the initial instability is not able to maintain and that the flow stays laminar from inlets to outlet. We have tried to destabilize this flow by applying pulsated forcing at the inlet with an \mathbf{u}_x 's amplitude of 50%, compared to the original inlet condition value (see equation (2)). No sign of transition was observed during all the computational time, the flow remains laminar. This laminar state is relatively resilient.

At this location, more specifically, this laminar non-Newtonian case NN_d^1 is characterized by $\mathbf{u}_z = 0$ during the computational time. On the contrary, for all the other cases, both the Newtonian and non-Newtonian at both DR and IR, \mathbf{u}_z fluctuates around zero. This means that an increase of inflow rate at both inlets breaks the plane of symmetry of flow structures and all four variables \mathbf{u}_x , \mathbf{u}_y , \mathbf{u}_z and c fluctuate. This is inherent to 3D turbulence. The transition between laminar state and a turbulent state in DR, appears between $\langle Re \rangle_{inlet} = 203$ ($Re_{PL}^{gen} = 329$) and $\langle Re \rangle_{inlet} = 449$ ($Re_{PL}^{gen} = 773$) for non-Newtonian fluid flow. According to our knowledge, there is no studies, showing whether instabilities should occur and develop, for a T-junction geometry, either for Newtonian or non Newtonian flow. However, in the case of JICF, some studies [38] show that the jet is stable for an inlet Reynolds number Re_{inlet} lower than a fixed critical Reynolds number $Re_c = 550$ for the case $r = 1.5$ and that such flow seems to become more stable when decreasing r i.e. the determined critical Reynolds number Re_c increases. It could be noted, that for our $r = 1$ cases and for non Newtonian cases, the critical Reynolds number for JICF, induced by [38]'s work, is largely greater than our inlet Reynolds numbers i.e. $Re_{inlet} > Re_c$. However, in the Nguyen's experimental work, when the same input rate is applied as in the case of NN_d^1 with $\langle Re \rangle_{inlet} \simeq 203$ ($Re_{PL}^{gen} = 329$), a turbulent state is observed. Possible reasons for experiment-simulation disagreement are : 1. In the experimental work a cylindrical T-junction is used. Curvature difference between circular and rectangular T-junction may have influence on stability. 2. Wall roughness is strictly zero in simulation whereas the roughness height is guaranteed only to be lower than $1\mu\text{m}$ in the experimental pipes. 3. The crossflow as well as the transversal jet are both laminar in simulations. In experiment fluctuations at various scales could persists at inlets in spite of upstream tranquilizing boxes $62.5D$ upstream. It is worth noting that Nguyen's experiment admits a 1% variation on flow rate measurement.

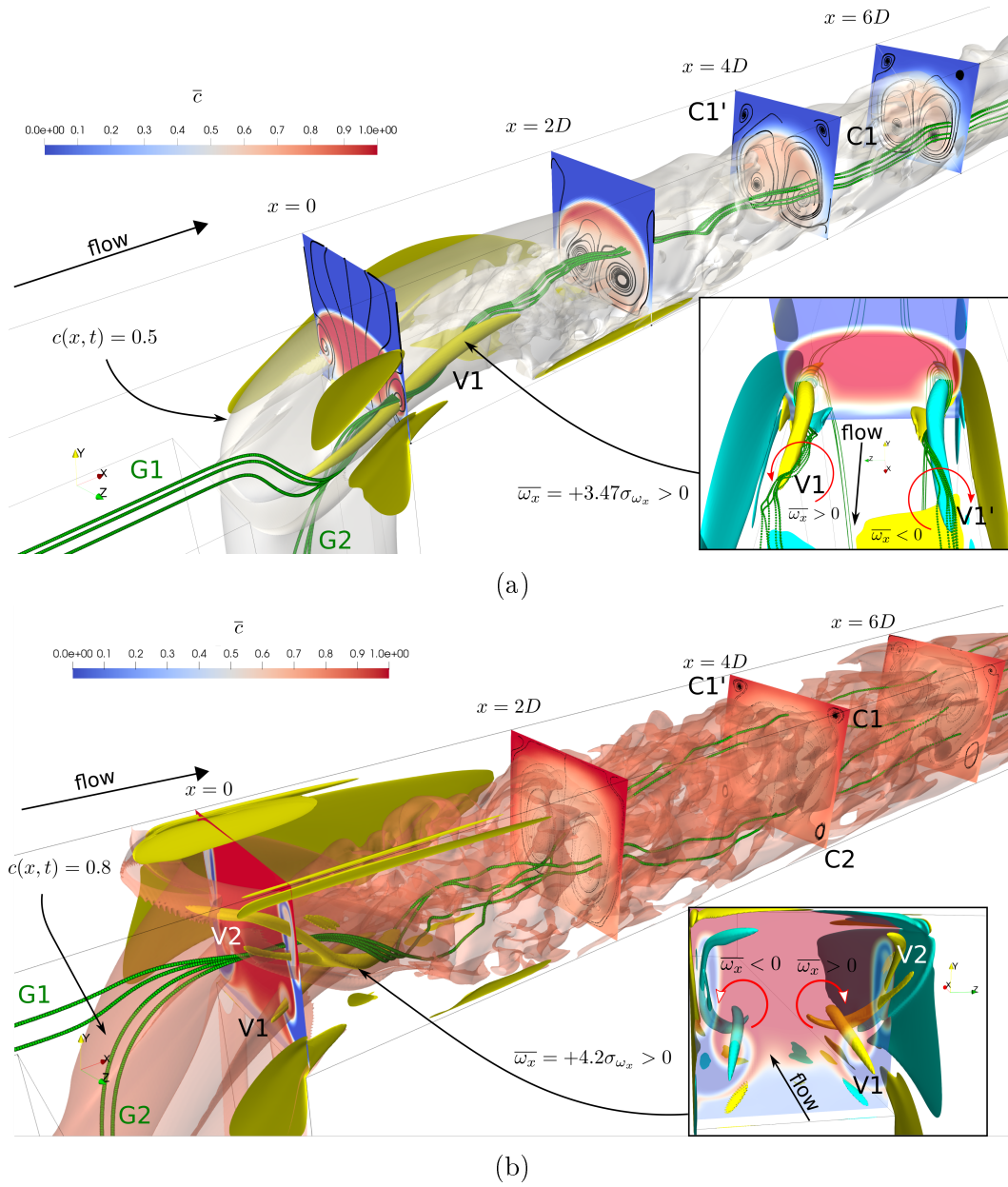


Figure 5: Illustration of the organization of the non-Newtonian flow for different regimes. (a) "deflecting" regime NN_d^2 (b) "impinging" regime NN_i^2 . See details in text.

3.2. Organization of the flow

In order to study the mechanisms that produce the mixing, we use Reynolds decomposition :

$$\mathbf{u} = \bar{\mathbf{u}} + \mathbf{u}', \quad (3a)$$

$$c = \bar{c} + c', \quad (3b)$$

$$\nu = \bar{\nu} + \nu', \quad (3c)$$

$$\boldsymbol{\omega} = \bar{\boldsymbol{\omega}} + \boldsymbol{\omega}' \quad (3d)$$

where we denote the time averaged component by adding a bar and the fluctuation component by adding a prime. Average operations are performed on the statistical stationary field (section 3.1). The structural organization of the flow for IR and DR regimes are illustrated on Figure 5 for case NN_d^2 and case NN_i^2 . Such a visualization of flow structures provides an overview of the impact of the flow regime on the scalar mixing.

In order to analyze the tri-dimensional organization of the flow, we plot several variables on Figure 5 for both DR and IR regimes. On Figure 5, to illustrate the concentration fluctuation, an iso-value of c is drawn in half-transparent white for $c = 0.5$ (NN_d^2) and in red for $c = 0.8$ (NN_i^2). The value $c = 0.5$ for IR or $c = 0.8$ for DR corresponds to the ideal mixing by taking into account the flow rate ratio $r = U_b/U_m$ (see section 4.3). The mean field \bar{c} is shown on the 4 transversal slices at $x/D = 0, 2, 4$ and 6 (where $x/D = 0$ corresponds to the downstream edge) in order to illustrate the diffusion of the scalar c by turbulence. This field is colored between red $\bar{c} = 1$ and blue $\bar{c} = 0$. Moreover, on the same slices, 2D streamlines (in black) are drawn based on 2D mean velocity (\bar{u}_y, \bar{u}_z) illustrating the 2D mean flow structures. Some particular streamlines are explicitly named $C1, C1'$ and $C2$. In addition, we superpose the iso-surfaces of the mean longitudinal vorticity field $\bar{\omega}_x$ to visualize the rotating vortices. The value of the iso-surfaces are taken as : $\bar{\omega}_x = +3.47\sigma_\omega$ for NN_d^2 and $\bar{\omega}_x = +4.2\sigma_\omega$ or NN_i^2 where σ_ω denotes the root mean square of $\bar{\omega}_x$ over the whole domain for respective cases. They are colored in yellow for positive vorticity $\bar{\omega}_x > 0$ and in cyan for negative vorticity $\bar{\omega}_x < 0$. The vortices and details are enlarged in the sub-frames in the direction of flow or in the opposite direction. Some particular vortices are explicitly named $V1, V1'$ and $V2$. Finally, tri-dimensional streamlines (in green) are added based on the instantaneous velocity field and named $G1$ from main duct and $G2$ from perpendicular duct.

Firstly, we observe that c fluctuates from the downstream edge till the exit showing a non-Newtonian turbulent flow in both deflecting and impinging regimes. In particular, for the DR case (NN_d^2), we observe a pair of counter-rotating swirling structures named $V1$ (yellow) and $V1'$ (cyan) on the zoomed figure 5 a) (only $V1$ on large figure). This pair ($V1, V1'$) is placed at the lower part of the square duct, close to the side wall corner and extend almost in the streamwise direction.

This structure in our non-Newtonian simulation is similar to Newtonian lower-deck steady kidney-vortices observed by Haven (figure 7 a) in [29]) for the JICF case and with a square nozzle. We extend the Haven's explanation to the non-Newtonian context : the non-Newtonian kidney vortices are originated from the sidewall boundary layer inside the

jet branch. It is also shown by 3D streamlines in green line ($G1$ and $G2$) that currents from both inlets exhibit firstly a motion in straight line, then deviate and are entrained by the rotating structures. The instantaneous passive scalar field also wraps around these structures and fluctuates. The existence of such kidney vortices near the junction plays as the motor of scalar pre-mixing in the DR regime. These vortices then break down to turbulence and enhance the ultimate mixing which occurs further downstream. Going further downstream, some persistent longitudinal corner vortices (named $C1$ and $C1'$) appear at the upper part of the square duct as shown in Gavrilakis's work on a periodic square duct [39].

On the other hand, for the IR case on zoomed figure 5 b), the transversal jet impacts the upper wall and a new vortex structure is organized from the upper corner and descends to the lower part of the duct. These descending vortices named $V2$ and the kidney-like vortices $V1$ as in DR case (NN_d^2), forms two co-rotating pairs ($V1, V2$) illustrated on sub-frames. To our knowledge, such mechanism with 3D descending rotating structure $V2$ is not yet studied even in Newtonian literature. The instantaneous passive scalar field and the 3D streamlines wrap around two pairs of co-rotating vortices ($V1, V2$). These rotating structures near the junction shall, like in previous case, enhance the pre-mixing. Corner vortices named $C2$ in the IR regime tends to grow larger than at the lower part of duct.

For non Newtonian fluid flows, DR and IR cases have very different flow structures. For a comparable flow regime (DR or IR), the non-Newtonian fluid flows tend to be more stable than the Newtonian fluid flows. We think that such differences will introduce a significant impact on the viscous core, the turbulence peak and the scalar mixing that will be discussed hereafter.

4. Effect of shear thinning on turbulence

4.1. Pressure drop and turbulence peak shifting

In order to describe deeper the turbulent properties of flows, we define the turbulent kinetic energy $k = \frac{1}{2}(\overline{\mathbf{u}_x'^2} + \overline{\mathbf{u}_y'^2} + \overline{\mathbf{u}_z'^2})$ by using velocity fluctuation components. The non-dimensionalized form is k/k_{max} where k_{max} (figure 6 a)) is the max value of k on the plane $z = 0$ for each case.

On figure 6 a) and b), we present k_{max} values and pressure drops for all different cases. We observe that for a same exit Reynolds number, $\langle Re \rangle_{exit}$ (see Table 2), the IR cases generate a much higher level of turbulence (characterised by the peak of k_{max}) than the DR cases do, both for Newtonian and Non-Newtonian fluid flows, i.e. (N_i^2 vs N_d^2) and (NN_i^2 vs NN_d^2). The specific vortex mechanisms, described in part (3.2), producing the turbulence, do not generate the same magnitude of turbulence. Indeed, in the IR cases, the jet impact the upper wall generating more background fluctuations (and an higher level of turbulence) that are redistributed downstream by the descending vortex $V2$ (shown on figure 5 b)). Moreover, for the same flow rate, the Newtonian cases have an higher turbulence levels than the corresponding non Newtonian fluid flows (N_i^2 vs NN_i^2) and (N_d^2 vs NN_d^2). It is consistent with the fact that $\langle Re \rangle_{exit}$ is higher in Newtonian cases than in Non-Newtonian case (see Table 2). This result is in agreement with preliminary experiment of Nguyen [31] using a circular-section T-junction.

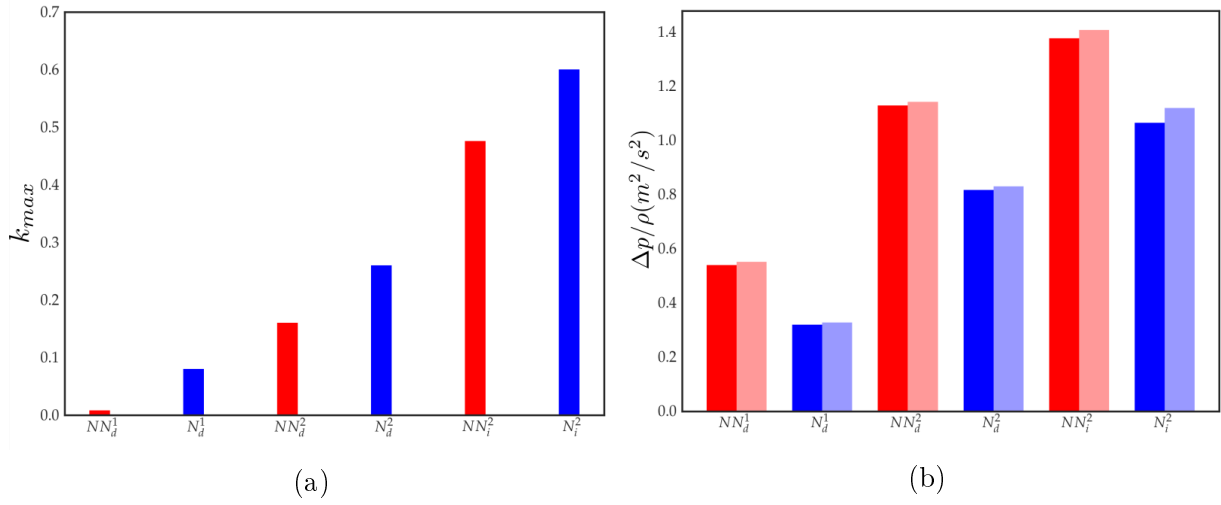


Figure 6: The two histograms for k_{max} and pressure drop : Red bars for non-Newtonian cases, blue bars for Newtonian cases. (a) The peaks of turbulent kinetic energy k_{max} on plane $z = 0$ for the six computed cases. (b) The associated pressure drops $\Delta p / \rho$. There are two columns for each case : opaque one for $\frac{p_{inlet} - p_{exit}}{\rho}$; transparent one for $\frac{p_{inlet} - p_{exit}}{\rho}$.

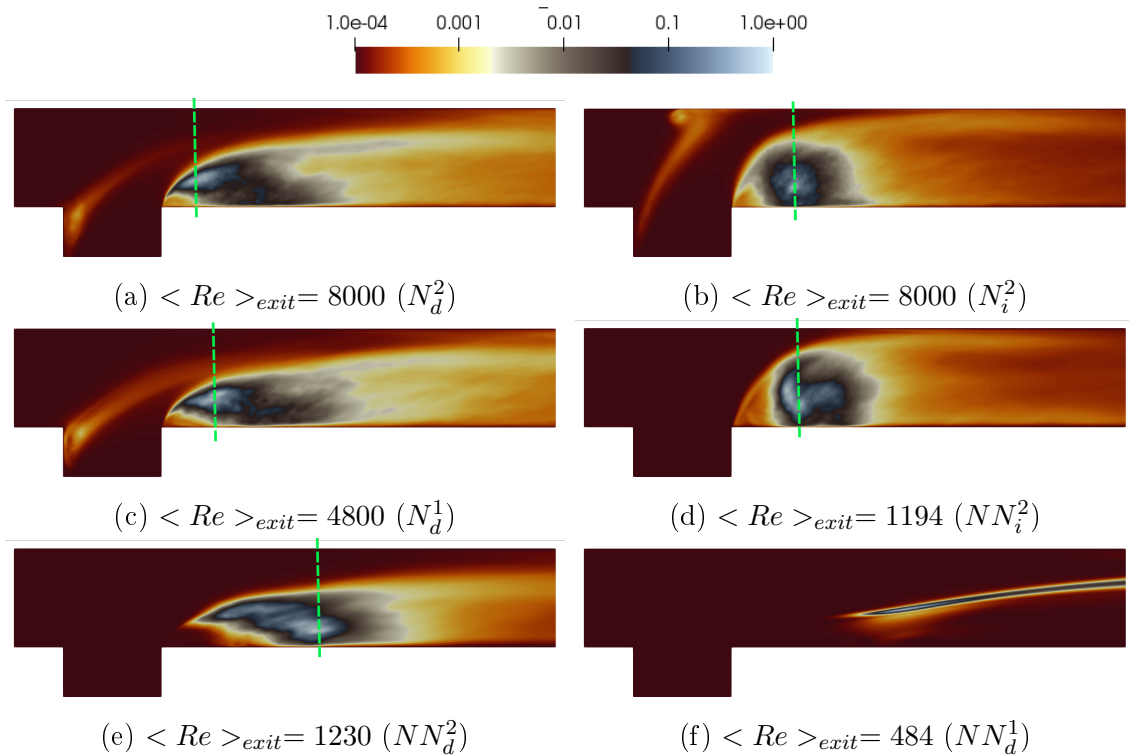


Figure 7: Contour plots of normalized kinetic energy k/k_{max} where k_{max} denotes the maximum turbulent kinetic energy on the slice $z = 0$.

For a given fluid (Newtonian or non Newtonian fluid), the increase of turbulent peak k_{max} comes at the price of an increased pressure drop over the T-junction (see Figure 6b)). This denotes also that pressure drop is a measure of dissipation. Given the same flow rate with the same $\langle Re \rangle_{exit}$ (Table 2) the IR cases are more expensive in term of pressure drop than the DR ones : 37% for non-Newtonian and 20% for Newtonian (NN_i^2 vs NN_d^2) and (N_i^2 vs N_d^2). This is of fundamental importance to have an a priori estimation on the energy cost for mixing processes.

However, the fluctuations due to turbulence are not uniformly distributed in the flow : intuitively, the location of the peak gives us information on the area that mix the most.

On figure 7, the spatial distributions of k/k_{max} are plotted for laminar (NN_d^1) and all other turbulent cases. For the laminar case (figure 7 f)), we found no perturbations generated from the downstream edge. The fluctuation k_{max} is negligible and concentrated in "a thin fluctuating band". It is actually part of the initial perturbation which is not yet convected to the exit neither fully dissipated. Due to computational cost, we stopped the calculation before its exit.

In the Newtonian DR cases, N_d^1 and N_d^2 (Figure 7 a) and c)), we have a similar distribution of k/k_{max} whereas the Reynolds number varies. The fluctuations appear from the downstream edge and are concentrated close to the bottom edge. Moreover, the higher fluctuations remain inside the re-circulation zone with a peak center whose location is indicated via a green dash line. From the peak, the fluctuations are rapidly (at a distance around $1D$) decreasing till 1% of the peak intensity. We call this region "intense turbulence zone" (ITZ) that could be visualized on figure 7 by the white boundary level (corresponding to levels around 0.2%) after black level color from the peak. Note that the ITZ is a part of the re-circulation zone for each case. Its location seems to be dependent on the exit Reynolds number : when $\langle Re \rangle_{exit}$ decreases from 8000 to 4800, the peak location is shifted toward the exit.

In contrast, for non-Newtonian turbulent DR case (NN_d^2 we can see on figure 7 e)) that the great values of k are much less concentrated compared to the Newtonian cases (N_d^2 and N_d^1 shown on figures 7 a) and c)). In addition, the position of the peak k_{max} is shifted further streamwise compared to the Newtonian cases. This is also confirmed in the preliminary Nguyen's work [31] with a circular-section T-junction. It seems to be a Reynold number dependance effect.

For the IR cases and both Newtonian N_i^2 (figure 7 b)) and non-Newtonian NN_i^2 (figure 7 d)) fluid flows the jet impacts the top wall inducing the ITZ to extend higher upward (to the top wall) and streamwise (to the exit) less further. In these cases, the distribution of the kinetic energy is similar inside the ITZ even if the exit Reynolds numbers $\langle Re \rangle_{exit}$ are different from 1194 to 8000 and no noticeable peak shifting is noted. Unlike, for the DR cases and for the same difference between the exit Reynolds numbers, difference as for the IR case, the ITZ's shape is similar but with a noticeable peak shifting (figures 7 a) to e)). This seems to indicate that the origin of the peak shifting is not related to a Reynolds number's effect but results from the shear thinning nature of the fluid.

4.2. From viscous core to turbulence and its relaminarization

By observing the contour plots of ν in figures 3 e) and f) (NN_d^2 vs NN_i^2), laminar flows are obtained, for each case, between the two inlets and the junction. In these zones, the maximum of viscosity ν_{max} is located at the center of ducts for both DR and IR where $\nu_{max} = 2.7 \times 10^{-4} m^2/s \approx \nu_0$. The center part is then characterized by an high viscosity, which is about 100 times more viscous than the viscosity close to the wall, of the same order than ν_∞ (figure 1b)) : we call this region the "viscous core". On the two plots, the viscous cores merge from the inlets inside the junction leading to turbulent flow in both cases. It is not obvious, a priori, that these highly viscous cores can be destabilized enough to generate a turbulent state that allows a more or less homogeneous mixing of the scalar transported from inlets 2. Indeed, an high viscosity tends to attenuate or prohibit any fluctuation and therefore any flow mixing (versus molecular one). In this section, we have characterized the spatial evolution of the viscous field from the junction to the outlet.

For all non-Newtonian cases, we show on figure 8a) several slices of the average viscosity field $\bar{\nu}$ demonstrating its evolution from the junction to the outlet. Slices are taken on a longitudinal plane $z = 0$ and several transversal planes $x/D = 0, 4$ and 8 where $x/D = 0$ corresponds to the downstream edge (the same kind of 2D vertical cuts are shown on figure 5 for $x/D = 0, 2, 4$ and 6). In order to describe the distribution of $\bar{\nu}$ on these transversal planes, we have also highlighted on figure 8b) the normalized histograms of $\bar{\nu}$. Moreover, on figures 9 a) and b) are shown the longitudinal evolution of the first two moments, of $\mu_{\bar{\nu}}(x)$ and $\sigma_{\bar{\nu}}(x)$, calculated for each x/D locations, to summarize the distribution of $\bar{\nu}$ on these transversal slices between the downstream edge at $x/D = 0$ and the outlet at $x/D = 10$. We use the average $\mu_{\bar{\nu}}$ and the standard deviation $\sigma_{\bar{\nu}}$ defined by :

$$\mu_{\bar{\nu}}(x) = \frac{1}{S(x)} \int_{S(x)} \bar{\nu} dy dz \quad (4a)$$

$$\sigma_{\bar{\nu}}(x)^2 = \frac{1}{S(x)} \int_{S(x)} (\bar{\nu} - \mu_{\bar{\nu}}(x))^2 dy dz \quad (4b)$$

If $\sigma_{\bar{\nu}}$ is small, then the distribution of $\bar{\nu}$ is almost homogeneous and concentrated around $\mu_{\bar{\nu}}$.

In the DR laminar case (i.e. NN_d^1), we observe that the average viscosity $\mu_{\bar{\nu}}(x)$ is high but constant up to $x/D \simeq 4$ like the standard deviation $\sigma_{\bar{\nu}}$. Above $x/D \simeq 4$, the standard deviation $\sigma_{\bar{\nu}}$ increases as the average viscosity $\mu_{\bar{\nu}}(x)$ increases. This behavior indicates that the viscosity is not homogeneous at $x/D \simeq 4$. Furthermore, on figure 8a), we can see that the center of the pipe is gradually occupied by a horseshoe-like structure constituted with fluid at high viscosity. This transversal structure is responsible for the non-homogeneity of the viscosity and therefore for the increase of the standard deviation.

In the DR and IR turbulent cases (i.e. NN_d^2 vs NN_i^2), the viscous cores are weaker in terms of $\mu_{\bar{\nu}}$ compared to the laminar case (see figure 9 a)). The moments $\mu_{\bar{\nu}}$ and $\sigma_{\bar{\nu}}$ grow monotonously from $x/D = 2$ and $x/D = 4$ for IR and DR. Their levels are lower than the laminar case. On the figure 8 a), we do not detect any particular structure. The viscosity field appears to be more homogeneous than for the laminar case.

The knowledge of the magnitudes of $\mu_{\bar{\nu}}$ and $\sigma_{\bar{\nu}}$ is not sufficient to correctly describe the spatial distribution of $\bar{\nu}$ (figure 8 b)). In particular, it is necessary to examine statistics of the points that have a local high viscosity. This local high viscosity is deduced and observed from the tails of the local (for each x/D) $\bar{\nu}$ histograms i.e. $\bar{\nu} > \mu_{\bar{\nu}} + \sigma_{\bar{\nu}}$. We define this extreme viscosity between high viscosity and low viscosity by :

$$\bar{\nu}_{ex} = \mu_{\bar{\nu}} + \sigma_{\bar{\nu}} \quad (5)$$

This choice is flow dependent because such reference $\bar{\nu}_{ex}$ varies from case to case and it is less arbitrary than if a unique threshold had been imposed for analysing. For example, for a Gaussian distribution of $\bar{\nu}$, 68% of points have a viscosity $\bar{\nu}$ in the range $[\mu_{\bar{\nu}} - \sigma_{\bar{\nu}}, \mu_{\bar{\nu}} + \sigma_{\bar{\nu}}]$ and thus only 16% of points have a viscosity $\bar{\nu}$ greater than $\bar{\nu}_{ex}$ (black dashed lines on figure 8 b)).

On figure 9 c), we observe that the evolution of $\bar{\nu}_{ex}(x)$, after a transition, has a global tendency to increase compared to its initial value $\bar{\nu}_{ex}(x = 0)$ for the three cases. We now quantify the percentage of points with an higher viscosity than $\bar{\nu}_{ex}(x = 0)$ by calculating the probability of having a high viscosity value with respect to the junction input $P(\bar{\nu} \geq \bar{\nu}_{ex}(x = 0))$ (figure 9 d)).

In the laminar case NN_d^1 , the percentage of points with an high viscosity doesn't fluctuate a lot and converges to 50%. This means that the distribution is extended to high viscosities. Unlike the turbulent cases (NN_d^2 and NN_i^2) which have their percentage of points close to 0% for IR and decrease until 4% for DR after a short transition to 18%. Their viscosity distributions is shrinking around low viscosities for the locations $0 \leq x/D \leq 6$. Such low percentage of high-viscosity points could help turbulence to develop in both IR and DR (NN_d^2 and NN_i^2) cases. This is consistent with the presence of a turbulence peak shown in the figures 7 d) and e) (shown by the green dashed line) compare to its absence for NN_d^1 (figure 7 f).

Above $x/D > 6$, the percentage of points with an high viscosity increases to 50% for both IR and DR cases : this is a sign of relaminarization of flow which prevents any fluctuation and therefore any efficient mixing. This is consistent with the large decrease levels of the turbulence fluctuations for the IR and DR cases shown on figures 7 d) and e) close to their outlets. As a conclusion, for the DR and IR turbulent cases (NN_d^2 and NN_i^2), the viscous core disappears right after the junction but a re-laminarization is expected close to the outlet at $x/D \simeq 6$ due to an increasing spatial domain with an high viscosity level.

4.3. Effect on mixing and quality of mixing

In this section, we quantify the passive scalar mixing from the junction to the outlet. As explained in section 2.2 we inject different values of passive scalar, ($c = 0$ at *inlet1* and $c = 1$ at *inlet2*). As noted in section 3, DR and IR have inherently different flow structures. This shall have a large impact on the scalar mixing whose result can be visualized by c -valued iso-surfaces' tilting and folding (figure 5(a) and (b)). As we did in the section 4.2, for the mean viscosity $\bar{\nu}$ (figure 8), we drew on figures 10 and 11 the contours and histograms of the scalar \bar{c} for the same transversal slices $S(x)$ evolving along the x -axis.

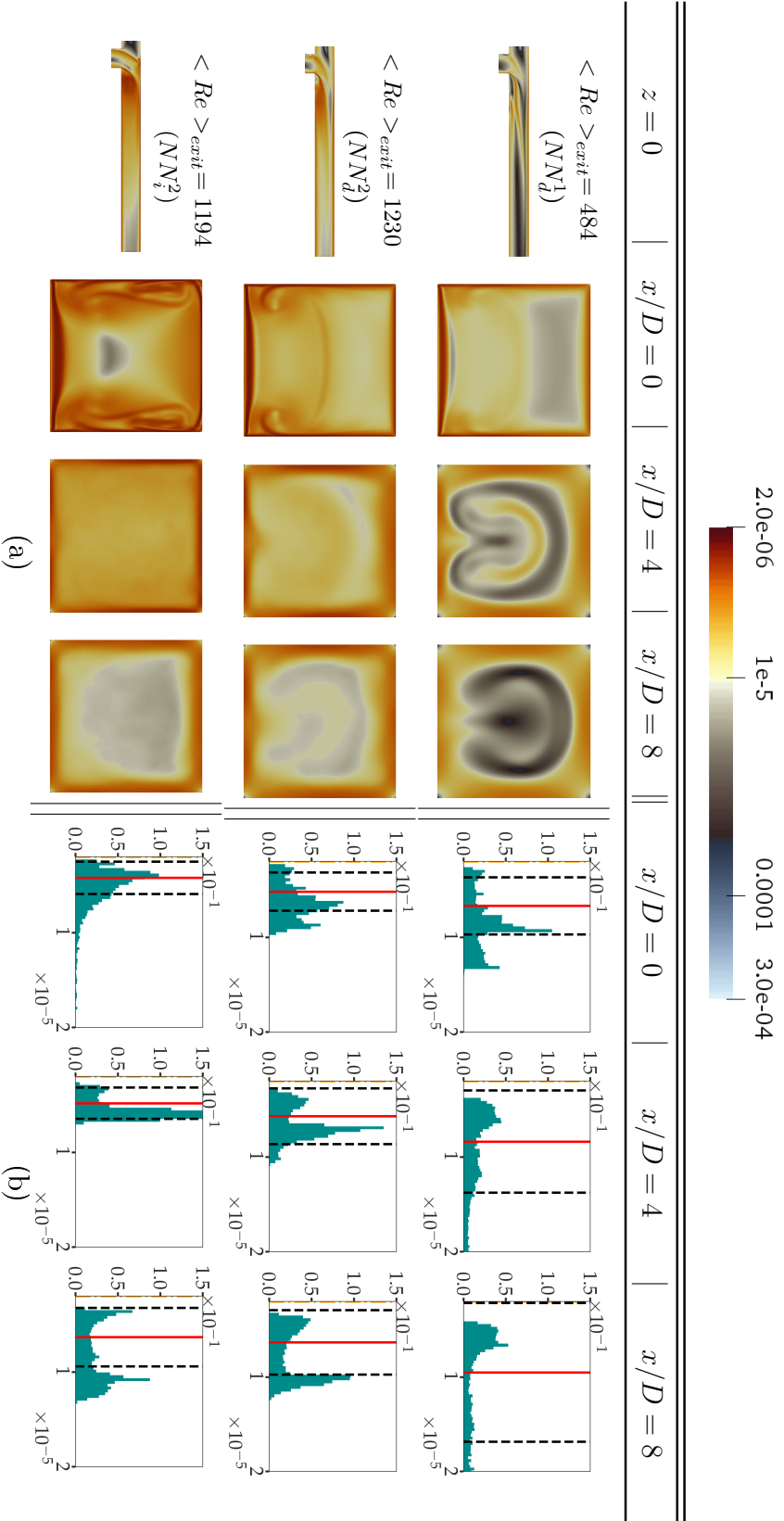


Figure 8: Contour plots and histograms on different vertical slices for average viscosity field $\bar{\nu}$ of non-Newtonian simulations. a) Contour plots of $\bar{\nu}$ on the vertical longitudinal plane $z = 0$ and the vertical transverse planes at $x/D = 0, 4$ and 8 . b) Normalized histograms of $\bar{\nu}$ on the previous vertical transverse planes. The Y-axis denotes frequency in percentage % and ranges from 0% to 15%. $bins$ are equally distributed between ν_∞ and ν_0 . The total number of $bins$ is fixed to be 1000. In figures only the interval $[\nu_\infty = 2e - 6, 2e - 5]$ is shown in order to have an optimal view. The Red line is for μ_{T7} and the black dashlines are for $\mu_{T7} \pm \sigma_{T7}$.

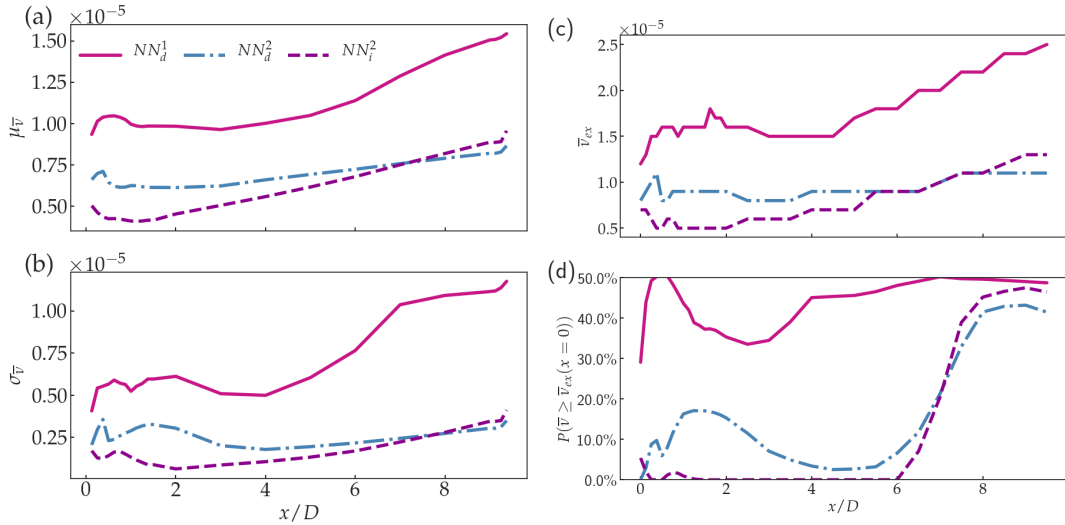


Figure 9: Evolution from the downstream edge $x/D = 0$ to the exit $x/D \approx 10$ of viscosity statistical parameters : average $\mu_{\bar{v}}$ (left top), standard deviation $\sigma_{\bar{v}}$ (left bottom), high viscosity value \bar{v}_{ex} (right top) and conditional probability $P(\bar{v} \geq \bar{v}_{ex}(x=0))$ of having an high viscosity value (right bottom) (all quantities defined in the text)

From a qualitative point of view, for the Non-Newtonian cases, an observation of the slices indicates that in the DR stable case (NN_d^1 (figure 10), the scalar is less mixed at the last location $x/D = 8$ than it is for the IR turbulent case (NN_i^2) (figure 11) at the same location.

In order to quantify the mixing, as done for the previous viscosity analysis (section 4.2), we use the spatial average of $\mu_{\bar{c}}(x)$ defined by :

$$\mu_{\bar{c}}(x) = \frac{1}{S(x)} \int_{S(x)} \bar{c} dy dz \quad (6)$$

This value $\mu_{\bar{c}}(x)$ should be compared with the value, \bar{c}_i , obtained in the case of an ideal mixing. Indeed, by taking into account the flow rate ratio r ($r = 1$ for the DR cases and $r = 4$ for the IR cases), the ideal mixing is expected to be $\bar{c}_i = \frac{r}{r+1}$ ($\bar{c}_i = 0.5$ for the DR cases and $\bar{c}_i = 0.8$ for the IR cases). However when such value is not reached everywhere, it is necessary to characterize the mixing quantifying the dispersion around the average value $\mu_{\bar{c}}$ [40]. We characterized it by the following standard deviation :

$$\sigma_{\bar{c}}(x)^2 = \frac{1}{S(x)} \int_{S(x)} (\bar{c} - \mu_{\bar{c}}(x))^2 dy dz \quad (7)$$

From these two quantities, the mixing tends to be qualified as homogeneous and ideal when $\mu_{\bar{c}}(x)$ is close to the ideal value \bar{c}_i and the standard deviation $\sigma_{\bar{c}}(x)$ is close to zero. The longitudinal evolutions of these quantities ($\mu_{\bar{c}}(x)$ and $\sigma_{\bar{c}}(x)$) have been plotted on figure 12 for each 6 cases.

For both turbulent IR cases, Newtonian and non-Newtonian fluid flows (NN_i^2 and N_i^2), $\mu_{\bar{c}}$ converges quickly ,along x , close to the ideal value as $\mu_{\bar{c}}(x) \simeq \bar{c}_i = 0.8$ (figure 12 a)).

Their standard deviations $\sigma_{\bar{c}}(x)$ converges also quickly to zero. The mixing is close to be ideal with an homogeneous scalar distribution. Such state is obtained almost at $x/D = 2.0$ (figures 12 a) and b)).

Note that for the Newtonian case (N_i^2) there is a better pre-mixing at $x/D = 0$ comparing to the non-Newtonian case NN_i^2 (see histogram on the figure 11). Nevertheless, for both cases, the scalar distribution is close to a Dirac-like distribution around the outlet at $x/D = 8$. Since the XG is initially more viscous than water, the fact that the mixing quality of the XG solution converge to the Newtonian situation after a short length (of $x/D = 2$), suggests that the flux in the non Newtonian case (NN_i^2) induces a very good pre-mixing. This could be affected to the presence of the near-junction vortex structure for this IR case (section 3.2). In this case the $\langle Re \rangle_{exit}$ is not relevant to qualify the mixing state because of the relaminarisation tendency (described in section 4.2).

Unlike, for the non-Newtonian laminar flow for the DR case (NN_d^1), the mean value is almost constant and close to the ideal value : $\mu_{\bar{c}}(x) \simeq \bar{c}_i = 0.5$. Nevertheless, its standard deviation $\sigma_{\bar{c}}(x)$ is comparable to its average, which means that the mixing remains heterogeneous and far from being ideal. This is probably due to the presence, from $x/D = 4$, of a \bar{c} horseshoe structure (figure 10 a)), corresponding to the one for the viscosity field $\bar{\nu}$ from the viscous core (figure 9). The high-viscosity horseshoe is so stable that it is transported downstream while preventing the velocity from fluctuating and thus any scalar fluctuation in the transverse direction of the flow. For this laminar case, this high-viscosity horseshoe-shaped structure prevents the flow to have a rapid good ultimate scalar mixing.

For the other DR turbulent cases, either for Newtonian (N_d^1 and N_d^2) or non-Newtonian (NN_d^2) fluid flow cases, the average $\mu_{\bar{c}}$ is almost constant and close to the ideal value $\mu_{\bar{c}}(x) \simeq \bar{c}_i = 0.5$. On the other hand, there is a difference in terms of dispersion between Newtonian and non-Newtonian cases. Indeed, for the Newtonian DR case N_d^1 , the standard deviation $\sigma_{\bar{c}}(x)$ tends slowly towards 0 compared to the turbulent IR case N_i^1 . By comparing both cases N_d^1 and N_d^2 , it seems that the Newtonian mixing, for DR situations and for this small range of Reynolds numbers, is rapidly independent of Reynolds number. Nevertheless, for the Non-Newtonian DR case NN_d^2 , the standard deviation $\sigma_{\bar{c}}(x)$ decreases much slower than for the corresponding Newtonian case N_d^2 . This means that the mixing is less efficient in the Non-Newtonian case than in the Newtonian case. Note that the mixing is delayed in the non-Newtonian case compared to the Newtonian case. This delay is illustrated by the scalar maps of the field \bar{c} : in the Newtonian case N_d^1 , the scalar map \bar{c} at slice $x/D = 4$ (figure 10) looks very similar, for the NN_d^2 case, to the slice at $x/D = 8$ (figure 11). The origin of this delay may not be linked directly to the level of the maximum turbulence peak k_{max} and its induced effects on mixing : on figure 6 a), the non-Newtonian flow case (NN_d^2) has a turbulence peak k_{max} comparable to the Newtonian flow case (N_d^1). Therefore this delay is mainly correlated with the downstream shifting (comparing both situations) of this turbulent peak and the fact that turbulence is in a less concentrated zone (section 4.1). Furthermore, for the non-Newtonian case, the re-laminarization at the output (section 4.2) prevents scalar fluctuations and therefore a good ultimate mixing is not expected further downstream.

By comparing non-Newtonian cases, for a same fixed outflow rate, in the DR case, NN_d^2 ,

the mixing is partially achieved at the output $x/D = 10$ while for the IR case, NN_i^2 , it is homogeneous at $x/D = 2$. Mixing is significantly enhanced passing from a DR to an IR.

The mixing quality can be further quantified by the factor $I_s = \frac{\sigma_{\bar{c}}}{Max(\sigma_{\bar{c}})}$ which is obtained by normalizing the dispersion by its maximum value, i.e at $x/D = 0$. This factor has already been used in the work by Sakowitz et al. [41] where the authors carried out Large Eddy Simulations (LES) for compressible gaz mixing study in a circular cross-section T-junction at a fully turbulent regime ($Re \approx 10^5$). The smaller the I_s factor is, the better the quality of mixing is. For the present study, the quality of the mixing follows generally the same trends as described above. The mixing quality is quickly achieved over a short distance in the IR case. Again, this result seems to be independent of the nature of the fluid (Newtonian or non-Newtonian) and of the Reynolds number $\langle Re \rangle_{exit}$ levels in the present range. The mixing quality is worse in the DR cases than in the IR cases that is consistent with the work by Sakowitz et al. [6]. In the DR cases, the mixing quality is achieved after a greater distance than for the IR cases. For the Newtonian DR cases, mixing quality appears to be independent of the Reynolds number $\langle Re \rangle_{exit}$ in our range of study. Nevertheless, whereas the mixing quality is the same from the junction ($x/D = 0$) to $x/D = 2$, it increases toward the outlet, more slowly for the non Newtonian case than for the Newtonian case. And the stable non Newtonian case has the worst mixing quality.

From a practical point of view, from the above observations, for the mixing of XG solutions, we will certainly favor the "impinging" regime rather than the "deflecting" regime for the same outgoing flow ($\langle Re \rangle_{exit}$). For the DR mixing, it is relatively difficult to obtain the ideal mixing $\bar{c}_i = 0.5$ with good homogeneity i.e. with low $\sigma_{\bar{c}}(x)$. Unlike for the IR mixing and $r = 4$, an ideal mixing will be obtained within a short distance with the expected value of $\mu_{\bar{c}} = 4/5$.

N.B. : To obtain the value $\mu_{\bar{c}} = 0.5$ in the "impinging" regimes, it is necessary to impose a scalar with a value $c = 5/8$ instead of $c = 1$ at the *inlet2*.

5. Conclusion and Perspective

In this work, flows in a square cross-section T-junction are investigated using Direct Numerical Simulation for different cases with a non-Newtonian inelastic fluid (Xanthan Gum solution) or Newtonian fluid (water) and different inlet velocity ratios. The shear-thinning property of the Xanthan Gum solution is modeled by the Bird-Carreau Law to correspond to experimental data by Nguyen [31]. The chosen lowest viscosity, ν_{∞} , limit of the non-Newtonian fluid is twice that of the Newtonian fluid. Note that we impose the same flow rates for Newtonian and non-Newtonian fluid flow even if the average Reynolds number at the inlet or outlet does not have the same order. Therefore, the Newtonian cases can be seen as the upper limit in terms of turbulent intensity, for the non-Newtonian cases. By introducing a passive scalar, we quantify mixing of the flow.

For non-Newtonian fluid flow, at relatively low nominal Reynolds number, both crossflow and transversal jet are laminar and carry a very viscous core before the junction. However, due to strong shear rate at the junction, the fluid viscosity decreases dramatically and a self-sustaining non-Newtonian turbulent flow is produced with specific properties comparing

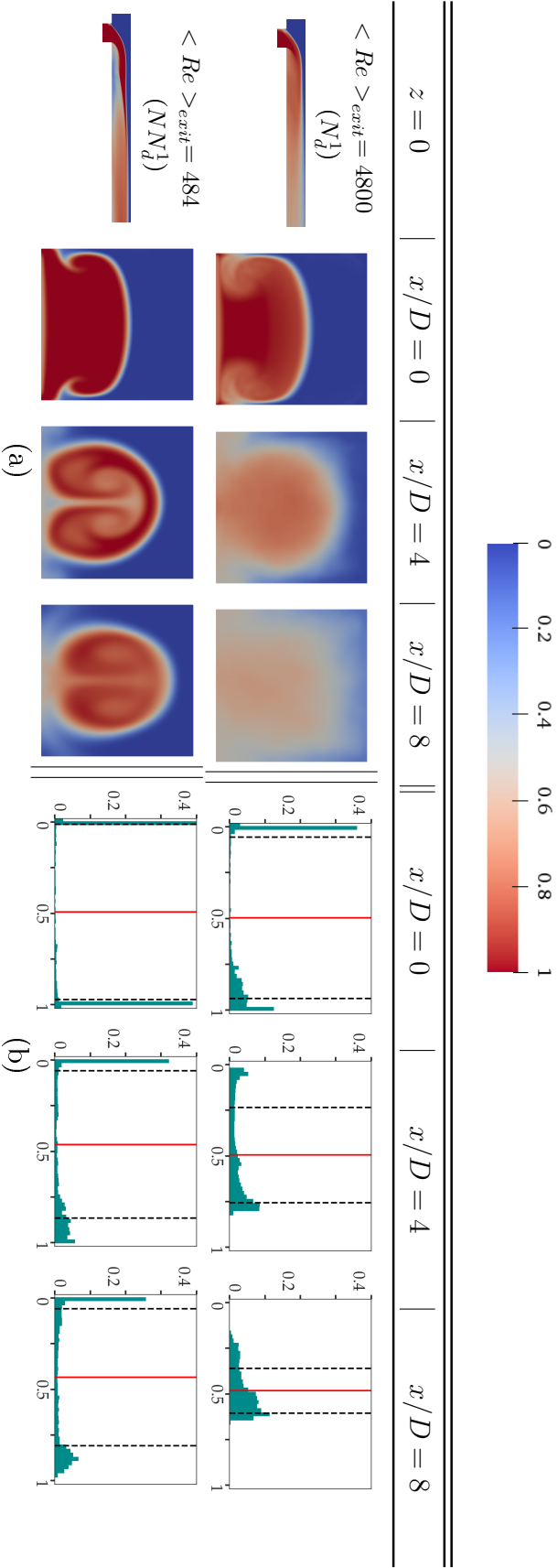


Figure 10: Contour plots and histograms of average concentration field \bar{c} for the low flow rate Newtonian N_d^1 and non-Newtonian NN_d^1 cases. a) Contour plots of \bar{c} on vertical plane $z = 0$ and vertical transverse planes at $x/D = 0, 4$ and 8 . b) Normalized histograms of \bar{c} on vertical transverse planes. Y-axis ranges from 0% to 40% denoting the frequency in percentage %. The Red line marks the position for $\mu_{\bar{c}}$ and the black dashed lines for $\mu_{\bar{c}} \pm \sigma_{\bar{c}}$.

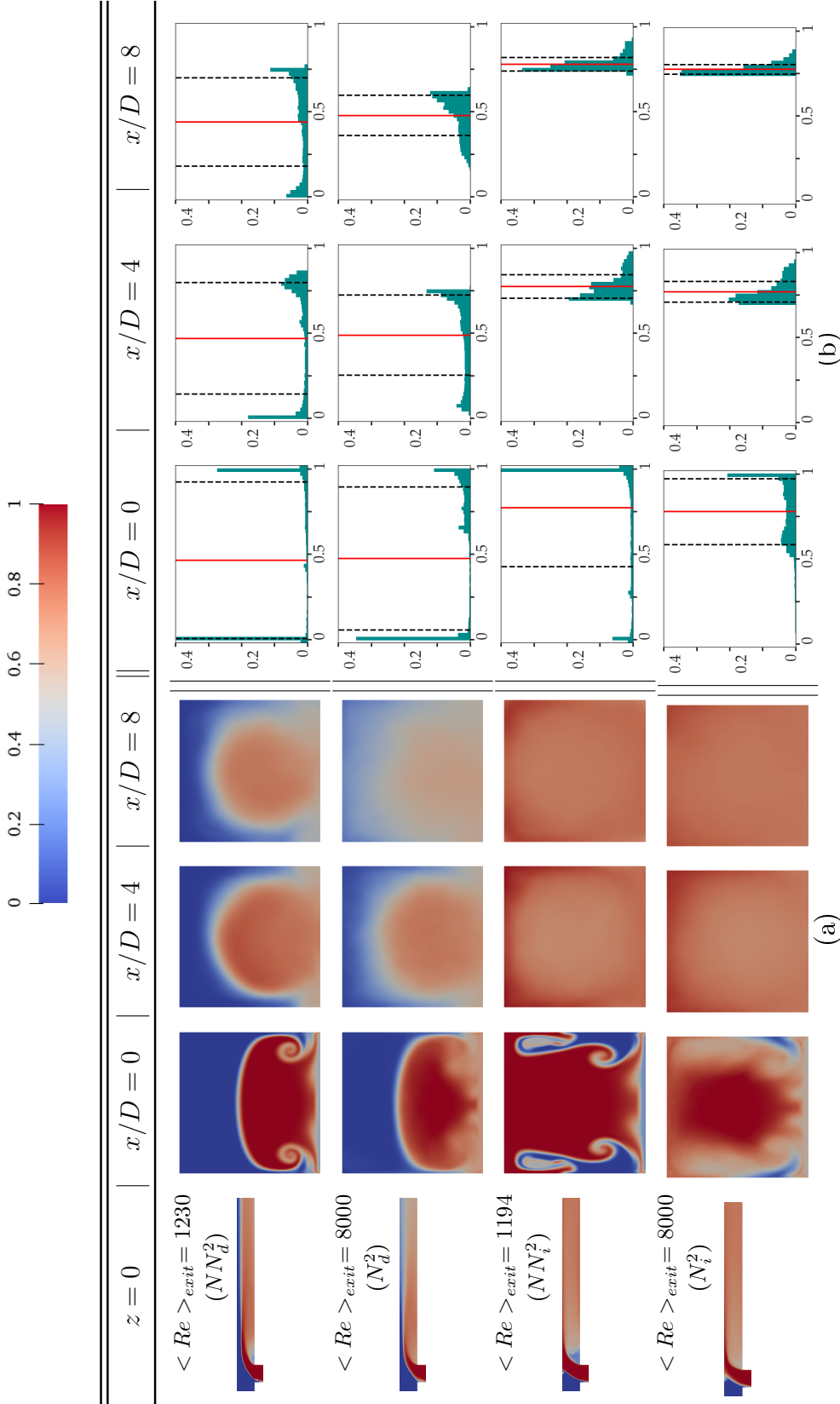


Figure 11: Contour plots and histogram of vertical slices for average concentration field $\bar{\tau}$ for higher flow rate Newtonian N_d^2, N_i^2 and non-Newtonian NN_d^2 and NN_i^2 cases. a) Contour plots of $\bar{\tau}$ on vertical plane $z = 0$ and vertical transverse planes at $x/D = 0, 4$ and 8 . b) Normalized histograms of $\bar{\tau}$ on vertical transverse planes. Y-axis ranges from 0% to 40% denoting the frequency in percentage %. The Red line marks the position for $\mu_{\bar{\tau}}$ and the black dashed lines for $\mu_{\bar{\tau}} \pm \sigma_{\bar{\tau}}$.

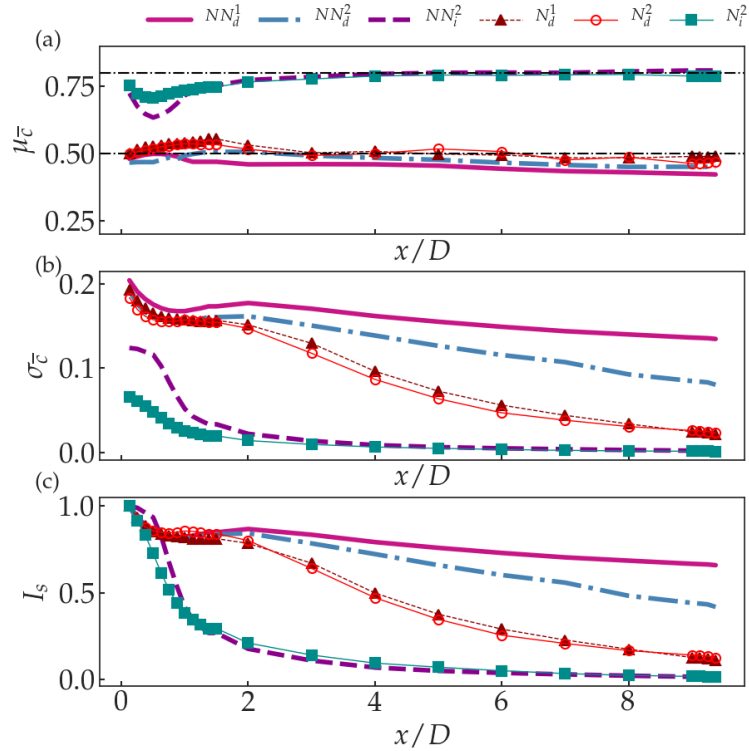


Figure 12: Longitudinal evolution of vertical transverse slice statistical parameters of the mean concentration field \bar{c} from the junction $x/D = 0$ to the outlet $x/D \approx 10$: average \bar{c} , root mean square $\sigma_{\bar{c}}$ and a mixing quality factor I_s (all defined in the text).

to the Newtonian case. Parameterized by the velocity ratio $r = U_b/U_m$, two flow regimes are investigated : the "deflecting" ($r = 1$, DR) and the "impinging" ($r = 4$, IR) regimes.

We have described the different vortex mechanisms that lead to the mixing. In the DR case, a non-Newtonian version of the kidney vortex pair, similar to the Newtonian "Jet In Cross Flow", is shown to be the motor of the scalar mixing. Furthermore, for the IR case, another downward vortex pair is added and significantly modifies the turbulent flow. This is due to the change of regime. This mechanism is new and have an impact on the quality of the mixing, in particular in the re-circulation zone. Such mechanism could probably be established in the Newtonian situations.

Unlike the IR case, for the DR one there is a displacement of the turbulent kinetic energy peak in the upper part of the recirculation zone with a widening of the fluctuating zone. It confirms the preliminary results from the experimental work of Nguyen [31] on a T-junction with circular cross section for DR cases.

For the non-Newtonian fluid flows , both for DR and IR cases, we demonstrate that a viscous core degenerates into turbulence at the junction and that a relaminarization zone appears with a high viscosity level that reduces fluctuations and mixing near the outlet ($x = 10D$ from the junction). The mixing is then restricted to a part of the junction. We show that at fixed flow rate, by switching from DR to IR, the non-Newtonian mixing is

considerably improved with a more efficient mixing obtained over a distance of $2D$ length from the junction. In addition, in the IR case, unlike the DR case, the mixing seems to be independent of the Reynold's number (in the studied range) and of the nature of the fluid.

The quantification of mixing quality provided in this work was initiated by the work of Nguyen [31] and other experimental or numerical works with circular cross-section T junction. It was conducted for both IR and DR in order to have a complete comparison for predicting the best mixing. For future works, it should be possible to compare more deeply and to extract some universal and non-universal properties of mixing in T-junction.

Investigating the viscoelastic response in the present geometrical configuration is also an interesting perspective. In particular, in the case of high elasticity regime, as with elastoinertial turbulence [42] (moderate Reynolds number) or elastic turbulence [43] (low Reynolds number), the mixing properties must change as a function of IR or DR, especially if pulsating input conditions are used.

Acknowledgements

Haining Luo is supported by the Chinese Scholarship Council (Fellowship #201504490098). This work was granted access to the HPC resources of CINES under the allocation A0042A10464 made by GENCI and HPC resources of the FLMSN, partner of EQUIPEX EQUIP@MESO.

Bibliography

- [1] O. Gelineau, C. Escaravage, J. P. Simoneau, C. Faidy, High cycle thermal fatigue: experience and state of the art in french lmfrs, in: Transactions of 16th International Conference on Structural Mechanics in Reactor Technology (SMiRT-16), Washington, DC, Aug, 2001.
- [2] J. C. J.P. Simoneau, O. Gelineau, Applications of large eddy simulations in nuclear field, in: 12th International Conference on Nuclear Engineering, 2004.
- [3] M. Hirota, E. Mohri, H. Asano, H. Goto, Experimental study on turbulent mixing process in cross-flow type t-junction, in: ICHMT DIGITAL LIBRARY ONLINE, Begel House Inc., 2009.
- [4] J. M. MacInnes, X. Du, R. W. K. Allen, Prediction of electrokinetic and pressure flow in a microchannel t-junction, *Phys. of Fluids* 15 (2003) 1992. doi:10.1063/1.1580479.
URL <https://doi.org/10.1063/1.1580479>
- [5] K. Krupa, M. Sultan, C. P. Fonte, M. I. Nunes, M. M. Dias, J. C. B. Lopes, R. J. Santos, Characterization of mixing in t-jets mixers, *Chemical Engineering Journal* (2012).
URL <http://www.sciencedirect.com/science/article/pii/S1385894712009539>
- [6] A. Sakowitz, M. Mihaescu, L. Fuchs, Effects of velocity ratio and inflow pulsations on the flow in a t-junction by large eddy simulation, *Computers & Fluids* 88 (2013) 374 – 385. doi:<https://doi.org/10.1016/j.compfluid.2013.10.001>.
URL <http://www.sciencedirect.com/science/article/pii/S0045793013003848>
- [7] A. I. P. Miranda, P. Oliveira, F. Pinho, Steady and unsteady laminar flows of newtonian and generalized newtonian fluids in a planar t-junction, *International Journal for Numerical Methods in Fluids* 57 (2008) 295 – 328. doi:10.1002/fld.1626.
- [8] H. Matos, P. Oliveira, Steady and unsteady non-newtonian inelastic flows in a planar t-junction, *International Journal of Heat and Fluid Flow* 39 (2013) 102 – 126. doi:<https://doi.org/10.1016/j.ijheatfluidflow.2012.11.005>.
URL <http://www.sciencedirect.com/science/article/pii/S0142727X12001415>

- [9] H. Matos, P. Oliveira, Steady flows of constant-viscosity viscoelastic fluids in a planar t-junction, *Journal of Non-Newtonian Fluid Mechanics* 213 (2014) 15 – 26. doi:<https://doi.org/10.1016/j.jnnfm.2014.08.015>.
URL <http://www.sciencedirect.com/science/article/pii/S0377025714001414>
- [10] R. I. Issa, P. J. Oliveira, Numerical prediction of phase separation in two-phase flow through t-junctions, *Computers & Fluids* 23 (2) (2010) 347–372.
- [11] P. M. Costa N. P., Maia R., P. F., Edge effects on the flow characteristics in a 90deg tee junction, *Journal of Fluids Engineering* 128 (6) (2006) 1204–1217.
- [12] H. C. Woolfenden, M. G. Blyth, Motion of a two-dimensional elastic capsule in a branching channel flow, *Journal of Fluid Mechanics* 669 (2011) 3–31. doi:[10.1017/S0022112010004829](https://doi.org/10.1017/S0022112010004829).
- [13] G. Y. Ahmed, A. Singh, Numerical simulation of particle migration in asymmetric bifurcation channel, *Journal of Non-Newtonian Fluid Mechanics* 166 (1) (2011) 42 – 51. doi:<https://doi.org/10.1016/j.jnnfm.2010.10.004>.
URL <http://www.sciencedirect.com/science/article/pii/S0377025710002685>
- [14] G. D’Avino, M. A. Hulsen, P. L. Maffettone, Separation of particles in non-newtonian fluids flowing in t-shaped microchannels, *Advanced Modeling and Simulation in Engineering Sciences* 2 (1) (2015) 9. doi:[10.1186/s40323-015-0033-9](https://doi.org/10.1186/s40323-015-0033-9).
URL <https://doi.org/10.1186/s40323-015-0033-9>
- [15] L. B. V. Khandelwal, A. Dhiman, Laminar flow of non-newtonian shear-thinning fluids in a t-channel, *Computers & Fluids* 108 (2015) 79 – 91. doi:<https://doi.org/10.1016/j.compfluid.2014.11.030>.
- [16] P. Neofytou, C. Housiadas, S. G. Tsangaris, A. K. Stubos, D. I. Fotiadis, Newtonian and power-law fluid flow in a t-junction of rectangular ducts, *Theoretical and Computational Fluid Dynamics* 28 (2) (2014) 233–256. doi:[10.1007/s00162-013-0311-4](https://doi.org/10.1007/s00162-013-0311-4).
URL <https://doi.org/10.1007/s00162-013-0311-4>
- [17] T. Burgehelea, E. Segre, I. Bar-Joseph, A. Groisman, V. Steinberg, Chaotic flow and efficient mixing in a microchannel with a polymer solution, *Physical Review E* 69 (6) (2004) 066305.
- [18] N. Fukushima, K. Fukagata, N. Kasagi, H. Noguchi, K. Tanimoto, Numerical and experimental study on turbulent thermal mixing in a t-junction flow (03 2003).
- [19] A. Kuczaj, E. Komen, M. Loginov, Large-eddy simulation study of turbulent mixing in a t-junction, *Nuclear Engineering and Design* 240 (9) (2010) 2116 – 2122, experiments and CFD Code Applications to Nuclear Reactor Safety (XCFD4NRS). doi:<https://doi.org/10.1016/j.nucengdes.2009.11.027>.
URL <http://www.sciencedirect.com/science/article/pii/S002954930900586X>
- [20] S. V. Haren, Testing dns capability of openfoam and star-ccm+ : In support of thermal fatigue assessment for complex geometries, Master’s thesis (2011).
- [21] M. Georgiou, M. V. Papalexandris, Direct numerical simulation of turbulent heat transfer in a t-junction, *Journal of Fluid Mechanics* 845 (2018) 581–614. doi:[10.1017/jfm.2018.256](https://doi.org/10.1017/jfm.2018.256).
- [22] J.-N. Tourvieille, R. Philippe, C. de Bellefon, Milli-channel with metal foams under an applied gas-liquid periodic flow: External mass transfer performance and pressure drop, *Chemical Engineering Journal* 267 (2015) 332–346.
- [23] L. Sroka, L. Forney, Fluid mixing with a pipeline tee: theory and experiment, *AIChE journal* 35 (3) (1989) 406–414.
- [24] H. Kamide, M. Igarashi, S. Kawashima, N. Kimura, K. Hayashi, Study on mixing behavior in a tee piping and numerical analyses for evaluation of thermal striping, *Nuclear Engineering and Design* 239 (1) (2009) 58 – 67. doi:<https://doi.org/10.1016/j.nucengdes.2008.09.005>.
URL <http://www.sciencedirect.com/science/article/pii/S0029549308004779>
- [25] R. J. Margason, Fifty years of jet in cross flow research, in: In AGARD, Computational and Experimental Assessment of Jets in Cross Flow 41 p (SEE N94-28003 07-34), 1993.
- [26] K. Mahesh, The interaction of jets with crossflow, *Annual review of fluid mechanics* 45 (2013) 379–407.
- [27] C. Brücker, Study of the three-dimensional flow in a t-junction using a dual-scanning method for three-dimensional scanning-particle-image velocimetry (3-d spiv), *Experimental thermal and fluid science* 14 (1) (1997) 35–44.

- [28] T. F. Fric, A. Roshko, Vortical structure in the wake of a transverse jet, *Journal of Fluid Mechanics* 279 (1994) 1–47. doi:10.1017/S0022112094003800.
- [29] B. A. Haven, M. Kurosaka, Kidney and anti-kidney vortices in crossflow jets, *Journal of Fluid Mechanics* 352 (1997) 27–64.
- [30] R. T. M’closkey, J. M. King, L. Cortelezzi, A. R. Karagozian, The actively controlled jet in crossflow, *Journal of Fluid Mechanics* 452 (2002) 325–335. doi:10.1017/S0022112001006589.
- [31] T. D. Nguyen, Influences des proprietes non-newtoniennes sur un melange de scalaire passif, Ph.D. thesis, thèse de doctorat de l’université de Lyon, délivrée par l’Ecole Centrale de Lyon (2013) (2013). URL <http://www.theses.fr/2013ISAL0084>
- [32] D. Jones, K. Walters, The behaviour of polymer solutions in extension-dominated flows, with applications to enhanced oil recovery, *Rheologica Acta* 28 (6) (1989) 482–498.
- [33] G. Axtmann, U. Rist, Scalability of openfoam with large eddy simulations and dns on high-performance systems, in: *High Performance Computing in Science and Engineering’ 16*, 2016.
- [34] J. Guerrero, Tips and tricks in openfoam, Tech. rep. URL <http://www.dicat.unige.it/guerrero>
- [35] N. A. Mortensen, F. Okkels, H. Bruus, Reexamination of hagen-poiseuille flow: Shape dependence of the hydraulic resistance in microchannels, *Physical Review E* 71 (5) (2005) 057301.
- [36] K. Madlener, B. Frey, H. Ciezki, Generalized reynolds number for non-newtonian fluids, *Progress in Propulsion Physics* 1 (2009) 237–250.
- [37] G. K. Batchelor, Small-scale variation of convected quantities like temperature in turbulent fluid part 1. general discussion and the case of small conductivity, *Journal of Fluid Mechanics* 5 (1) (1959) 113–133.
- [38] J. Blanchard, Y. Brunet, A. Merlen, Influence of a counter rotating vortex pair on the stability of a jet in a cross flow: an experimental study by flow visualizations, *Experiments in fluids* 26 (1-2) (1999) 63–74.
- [39] S. Gavrilakis, Numerical simulation of low-reynolds-number turbulent flow through a straight square duct, *Journal of Fluid Mechanics* 244 (1992) 101–129.
- [40] E. Villermaux, Mixing versus stirring, *Annual Review of Fluid Mechanics* 51 (2019) 245–273.
- [41] A. Sakowitz, M. Mihaescu, L. Fuchs, Turbulent flow mechanisms in mixing t-junctions by large eddy simulations, *International Journal of Heat and Fluid Flow* 45 (2014) 135 – 146. doi:<https://doi.org/10.1016/j.ijheatfluidflow.2013.06.014>. URL <http://www.sciencedirect.com/science/article/pii/S0142727X13002099>
- [42] Y. Dubief, V. E. Terrapon, J. Soria, On the mechanism of elasto-inertial turbulence, *Physics of Fluids* 25 (11) (2013) 110817.
- [43] A. Groisman, V. Steinberg, Elastic turbulence in a polymer solution flow, *Nature* 405 (6782) (2000) 53.